



Brinkman double-layer model for flow at a free-porous interface

Jinliang Kang, Moran Wang*

Department of Engineering Mechanics, Tsinghua University, Beijing, 100084, China

ARTICLE INFO

Keywords:

Porous media
Stokes–Darcy flow
Brinkman model
Interface conditions
Lattice Boltzmann method

ABSTRACT

The phenomenon of the Stokes–Darcy flow in coupled systems comprising a clear channel and a complex 3D porous medium is investigated through both numerical and theoretical approaches. A quartet structure generation set (QSGS) method is used to generate random complex 3D porous structures imitating real structures in nature. Pore-scale flow simulations are performed using the Lattice Boltzmann method, enabling detailed analysis and characterization of the interfacial flow phenomena. Four key parameters with clear physical meanings are introduced to quantitatively capture essential aspects of the flow dynamics, revealing intriguing linear relationships with the square root of permeability – a fundamental characteristic length scale dominating the phenomenon. Several existing models are examined by these parameters. To address the limitations of existing models, a Brinkman double-layer (BDL) model is proposed. By comparing with several classic models, the present BDL model stands out due to its simplicity, accuracy and robustness, providing a comprehensive understanding of the complex flow behavior in the coupled system.

1. Introduction

Permeable boundaries are prevalent in both natural and industrial settings. The coupled flow system containing a free-fluid region and fluid-saturated porous bed finds extensive applications in various fields such as lubrication with porous bearings [1], interfacial heat transfer [2,3], geothermal operations [4,5], nuclear waste repositories [6,7], underground coal gasification [8], groundwater hydrology [9], and biological transport processes [10]. The inclusion of permeable boundaries, as opposed to solid walls, introduces significant distinctions in bulk flow behavior due to intricate fluid–solid interactions and momentum exchange across the free-porous interface.

The exploration of fluid flow within the free-porous coupled systems dates back to the 1950s when early investigations on fluid flow confined by porous walls or rollers [11,12] were conducted. Later, a significant milestone in this field was achieved by Beavers and Joseph [13], who conducted an influential experiment using a binary channel configuration comprising a long, naturally permeable block and a small, uniformly spaced gap atop it. By measuring the total flow rate with various fluids featuring distinct porous structures, they derived an empirical equation that connected Darcy flow within the porous region and Stokes flow within the channel as $\frac{du}{dy} = \frac{\alpha}{\sqrt{K}}(u_B - Q)$. Here, K denotes the permeability of the porous material, u_B represents the slip-flow velocity at the interface, Q indicates the filtration velocity within the porous medium, and α represents a dimensionless quantity influenced by material properties. This equation is commonly referred

to as the Beavers–Joseph boundary condition, or the B-J model, and has since been widely employed by researchers. Subsequently, Saffman provided a theoretical basis for the Beavers–Joseph model (B-J model) by deriving a simplified equation known as the Beavers–Joseph–Saffman (B-J-S) boundary condition [14]. Numerous subsequent studies have focused on analyzing and deriving theoretical expressions for α , as well as proposing modifications to the B-J model [15,16]. Despite the widespread adoption of the B-J model, several studies have highlighted its limitations [17,18]. These deficiencies include the high sensitivity of α to the definition of the nominal interface, the substantial difference between Darcy filtration velocity and Darcy velocity near the interface, and its failure to accurately represent certain scenarios. Despite these drawbacks, the B-J model remains widely employed in various fields due to its inherent simplicity [3,19–22].

A significant limitation of the B-J model is its reliance on the Darcy equation to describe flow within porous media. Since Darcy's Law is only applicable to flow within the bulk portion of porous media, it fails to capture flow behavior near boundaries. Neale and Nader [23] addressed this limitation by incorporating Brinkman's extension of Darcy's Law within the porous media, resulting in a model that ensures fluid velocity continuity across the free-porous interface. Neale's model demonstrated that the interfacial fluid velocity obtained was equivalent to the slip velocity predicted by the B-J model, and the dimensionless parameter α in the B-J model represented the square root of the ratio of effective viscosity to fluid viscosity. Subsequent researchers further

* Corresponding author.

E-mail address: mrwang@tsinghua.edu.cn (M. Wang).

Nomenclature

c	Dimensionless parameter in B-W model
c_i	Lattice speed
f_i	Boltzmann particle density distribution function
H	Channel height
K	Permeability
L	Particle side length
M	Transformation matrix
p	Pressure
S	Relaxation-time matrix
u	Fluid velocity
u_{Darcy}	Darcy velocity
u_s	Slip velocity
α	Dimensionless parameter in B-J model
β	Dimensionless parameter in O-W model
$*\beta$	Physical value in fluid phase
$\langle *\beta \rangle^\beta$	Intrinsic average
$\langle *\beta \rangle$	Superficial average
γ	Dimensionless parameter in present BDL model
δ	Interface layer thickness
Δt	Time step
Δx	Lattice size
ε	Porosity
η	Clean channel
μ	Fluid viscosity
$*\sigma$	Physical value in solid phase
τ_{channel}	Shear stress from the side of clean channel
τ_{dif}	Shear stress difference
τ_{porous}	Shear stress from the side of porous media
ω	Porous medium
Ω_i	BGK collision operator

refined and validated this model [24,25]. However, it is important to note that the modeling results were not universally satisfactory, and the Brinkman equation itself exhibited certain deficiencies, such as overestimating seepage velocity and being inapplicable to certain types of porous media [26,27]. The above results implies that a single exponential curve described by the Brinkman equation is not enough to capture the flow dynamics in the porous media, and other governing equations may be required.

Notably, researchers have identified a narrow zone in the porous medium near the interface, characterized by a rapid decay in fluid velocity [28,29]. This critical zone has been previously referred to as the “boundary layer” or “transition layer” [30,31]. In response, Bars and Worster [30] proposed a model in which the thickness of this zone acted as a parameter, yielding satisfactory results [32]. Referred to as the B-W model, their approach employed the Stokes equation, rather than the Darcy equation, to describe flow within this zone. The B-W model assumed both velocity and velocity gradient continuity across the free-porous interface. However, the continuity of the velocity gradient (or shear stress) across the interface remains uncertain and necessitates further investigation.

Over the past decades, extensive research has been conducted through numerical simulations and experimental studies to explore novel flow patterns across free-porous interfaces. Previous numerical simulations primarily employed 2D porous structures composed of regular arrays, with porosity values typically exceeding 0.5. Examples of such structures include arrays of circular cylinders [26,33],

ellipses oriented in various directions [34,35], square prisms [36], and surface textures [37]. In contrast, the number of experimental studies conducted on this topic remains relatively limited. Given the inherent difficulty of directly measuring velocity profiles within natural porous media, experiments often employed simplified regular porous structures, such as packed glass beads [38,39] or arrays of rectangular or circular pillars [40,41]. Utilizing Modern optical techniques like Laser Doppler Anemometry (LDA) [42] and Particle Image Velocimetry (PIV) [43], a few researchers suggested that the thickness of the “transition layer” is proportional to the size of the solid obstacles, such as glass beads [38] and cylindrical rods [40]. However, the velocity profiles exhibited wavy patterns due to structural regularity. Although these patterns can be mitigated by averaging technique, recent studies have highlighted additional errors in this smoothing process [44]. Moreover, the inherent regularity of porous structures poses challenges in establishing a comprehensive and universally applicable law governing flow behavior within such coupled systems.

The lattice Boltzmann method (LBM), a high-efficiency pore-scale simulation method, has been rapidly developed in the last few decades [45,46]. Unlike traditional continuum-based fluid mechanics approaches, LBM is a mesoscopic method based on the Boltzmann transport equation. Through the Chapman–Enskog multiscale analysis, the Boltzmann equation can recover the macroscopic governing equations of fluid dynamics [47,48]. LBM offers significant advantages in handling complex boundary conditions [49,50] and parallel computing [51], rendering it an ideal tool for modeling flow in large-scale porous media with complex geometries [52]. Thus, LBM makes it convenient to study the flow behaviors in free-porous coupled systems with complex 3D porous structures numerically.

Upscaling techniques are commonly employed to derive macroscopic models, which can be broadly classified into two categories: the one-domain approach [53] and the two-domain approach [54]. The one-domain approach utilizes a single set of governing equations to model momentum transport throughout the entire system, for example, the heuristic combination of the Navier–Stokes (N-S) equation with the Darcy term [55]. Consequently, the effective properties such as permeability and porosity become position-dependent, necessitating the solution of complex auxiliary closure problems [56]. In contrast, the two-domain approach involves coupling different governing equations in the clean channel and the porous medium through additional interfacial conditions, yielding great simplification to the solution process.

The multiscale asymptotic method and the volume-averaging method stand as the two most widely adopted upscaling approaches. The multiscale asymptotic method assumes high periodicity in the porous medium, which are decomposed to elementary cells of the pore size. Through asymptotic expansion, approximations of different orders are constructed. Additional auxiliary problems are introduced to establish closure formulations and fulfill specific physical requirements [57], yielding complex parameters whose theoretical expressions are practically infeasible to apply in real rocks [58–60]. Though progress has been made recently in random 2D patterns [61], these patterns still differ from natural structures significantly, necessitating further investigation. In contrast, the volume-averaging method is simpler and more physically grounded. Based on the homogeneity assumption, this method take the mean value of physical field in a representative elementary volume (REV) as the superficial volume-averaged value, and decomposes values at other points into this mean value and fluctuations. This method facilitates the derivation of the volume-averaging form of the flow equations [62]. Utilizing the volume-averaging method, Ochoa-Tapia and Whitaker [54] introduced interfacial conditions (referred to as the O-W model) encompassing a velocity-continuity condition and a stress-jump condition, connecting the Stokes equation in the free channel with the Brinkman equation in the porous medium. This O-W model involves a model parameter β , which represents a complex function dependent on various

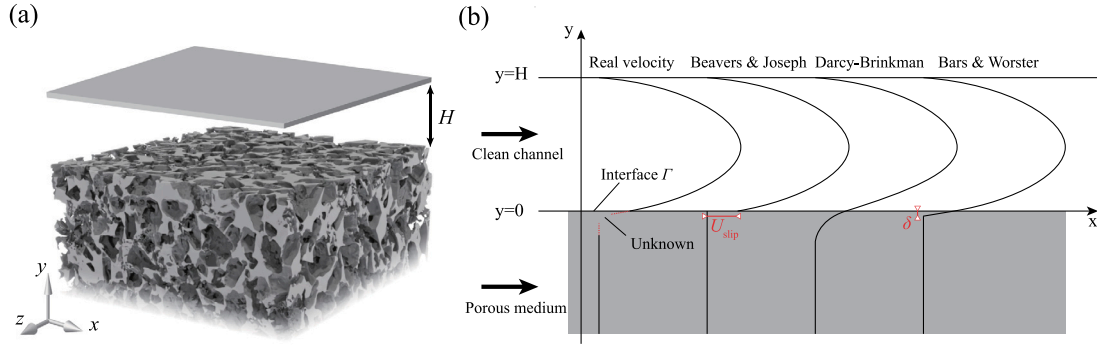


Fig. 1. Schematic illustration of (a) the coupled flow system consisting of a clean channel and a porous medium and (b) real velocity distribution and results of different models. The system is bounded by the upper solid wall. The height of the channel is denoted by H .

parameters [63,64]. Models developed using this method must adhere to specific length-scale constraints [65] and typically incorporate complex parameters that must be experimentally determined [56,66]. Recently, Ochoa-Tapia et al. [44] identified another potential drawback, whereby the averaging processes across the interface may give rise to artificial transition layers.

In this work, we provide comprehensive quantitative understanding and modeling of the primary flow mechanics in the free-porous coupled flow systems as sketched in Fig. 1. Pore-scale direct simulations are performed in such flow systems and four characteristic parameters are proposed to capture the main flow dynamics quantitatively. A new model comprising a new stress-jump interface condition and a novel double-layer structure is proposed and examined by the four parameters, together with several classic models. This paper is organized as follows. §2 provides an overview of the numerical methods employed, including the stochastic structure generation method and the lattice Boltzmann method (LBM). In §3, four key parameters are proposed to characterize the behaviors of the interfacial flow and their variations in response to structure permeability are summarized. Several existing models are examined by these parameters. §4 is dedicated to presenting our new Brinkman double-layer model. We present a comparative analysis of this model with simulation results and existing models, highlighting its advantages. Finally, the conclusions are summarized in §5.

2. Pore-scale simulation method

This section presents the numerical methods employed for conducting pore-scale simulations in free-porous coupled flow systems. These systems consist of complex 3D porous structures, which mimic real structures found in nature. The numerical methods involve the generation of random porous structures with varying porosity and permeability values, as well as a lattice Boltzmann method (LBM) [47] to solve the governing equations.

The quartet structure generation set (QSGS) method is utilized to generate the porous components of the coupled systems for pore-scale simulations. This method, proposed by Wang et al. [67], Wang and Pan [68], is inspired by the stochastic cluster growth theory and enables the generation of complex microstructures that closely resemble realistic porous media. To successfully generate representative microstructures, three statistical parameters are required as inputs: porosity, average grain size, and the degree of isotropy of the porous medium. In this work, a periodic boundary condition is employed in the QSGS method to ensure uniform porosity throughout the boundary region and the bulk porous medium. Further details regarding the QSGS method are provided in Appendix A.

In this study, homogeneous granular porous microstructures were generated using the QSGS method, considering a range of porosity values from 0.2 to over 0.9. For each porosity value, five cases with

different average grain sizes are considered, denoted as largest, large, medium, small, and smallest grain size. Additionally, we generate several high-porosity structures ($\epsilon > 0.9$) with extremely large cluster sizes to simulate extreme conditions. Given the stochastic nature of the generation method, we generate more than three individual microstructures (ten for benchmarking purposes) for each porosity and grain size combination to ensure statistical reliability. The size of the generated porous structures is intentionally chosen to be significantly larger than the average pore size, which is measured using the maximum ball method [69]. This ensures that the generated structures satisfy the representative elementary volume (REV) scale requirement and minimizes fluctuations caused by accidental large pores. Finally, each generated microstructure is combined with a clean straight channel to construct the desired coupled flow system.

The lattice Boltzmann method (LBM), a high-efficiency pore-scale simulation method, is employed to model fluid flow in the coupled systems. Though LBM is based on the mesoscopic Boltzmann transport equation, it can recover the Navier–Stokes equation through the Chapman–Enskog multiscale analysis [47,48]. Thus, LBM provides an alternative strategy for solving the N-S equation in both the clean channel and the pores of the porous media.

LBM offers several significant advantages, including its efficient handling of complex boundary conditions, such as porous media [49, 50,70]. This method excels in implementing intricate boundary conditions due to its local nature, where most of the evolution quantities are computed locally on a lattice. Moreover, LBM exhibits excellent scalability and is highly amenable to parallel computing [51], enabling the simulation of large-scale problems. This parallelizability makes LBM particularly suitable for modeling complex systems involving porous media.

In LBM, the velocity space is discretized by certain velocity sets, like the D3Q19 scheme used in this paper. In the discretized space, the lattice Boltzmann equation (LBE) reads as follows

$$f_i(\mathbf{x} + \mathbf{c}_i \Delta t, t + \Delta t) = f_i(\mathbf{x}, t) + \Omega_i(\mathbf{x}, t), \quad (1)$$

where $f_i(\mathbf{x}, t)$ is the Boltzmann particle density distribution function at position \mathbf{x} in time t , \mathbf{c}_i is the lattice speed defined as $\mathbf{c}_i = \Delta \mathbf{x} / \Delta t$, where $\Delta \mathbf{x}$ is the lattice size and Δt is the time step, and Ω_i stands for the collision operator. Based on this equation, the evolution of the density distribution function can be decomposed into two steps: streaming and collision. In the streaming part, the populations propagate to neighboring nodes along the velocity directions. In the collision part, the populations at each lattice node relax towards the equilibrium distributions. The single-relaxation-time (SRT) model for LBM with the Bhatnagar–Gross–Krook (BGK) collision operator is used in this work for a given viscosity:

$$\Omega_i(f) = -\frac{f_i - f_i^{eq}}{\tau} \delta t. \quad (2)$$

The relaxation time τ is a function of the kinetic viscosity ν of fluid as follows

$$\tau = \frac{3\nu\Delta t^2}{\Delta x^2} + \frac{\Delta t}{2}. \quad (3)$$

The SRT-LBM works well only when the dimensionless relaxation time $\tau/\Delta t$ is within (0.5, 2) and may get unstable when $\tau/\Delta t$ approaches 0.5, which essentially constrains the capability of this method. In this research, the relaxation time for SRT-LBM was set to 1 for all cases. For fluids with a wide range of viscosity, we further employ the multiple-relaxation-time(MRT) scheme of LBM [71] for better stability and robustness. The evolution equation of MRT-LBM becomes

$$f(\mathbf{x} + c_i\Delta t, t + \Delta t) - f(\mathbf{x}, t) = -\mathbf{M}^{-1}\mathbf{S}\mathbf{M} [f(\mathbf{x}, t) - f^{\text{eq}}(\mathbf{x}, t)] \Delta t, \quad (4)$$

where \mathbf{M} is the transformation matrix through which populations are transformed from population space to moment space. \mathbf{S} is a diagonal matrix called the relaxation-time matrix. The relaxation-time matrix contains multiple relaxation values, which allow each moment to be relaxed at individual rates. To ensure the truncation errors are identical for different values of viscosity, further constraints have been added to the relaxation-time values [72].

To validate the accuracy and capability of our LBM codes, we perform simulations of various flow scenarios. Results show that our framework has a second-order accuracy and is capable of simulating flow in complex porous media with various values of fluid viscosity. Details of the validations are introduced in [Appendix B](#).

For pore-scale modeling in the coupled system ([Fig. 1\(a\)](#)), non-slip boundary conditions are imposed on the solid surfaces, including the upper solid wall and the solid surfaces of the pores in the porous medium. The widely used bounce-back boundary condition has been implemented to handle the complex geometries in the generated porous media. For the inlet and outlet boundaries, a non-equilibrium pressure boundary condition [73] is utilized, with some appropriate modifications [74,75]. The remaining boundaries are treated as periodic boundaries. Gravity effects are neglected in this study. These boundary conditions are carefully selected to accurately represent the physical behavior of the system under investigation.

3. Assessment of existing models

In this section, pore-scale simulations are conducted in free-porous coupled systems featuring complex 3D porous structures, by which several existing models are examined. Four key factors quantitatively characterizing the interfacial transport phenomena are summarized, and their variations with respect to the structure morphology are analyzed.

To bridge the scale gap between the pore and Darcy scales, a volume-average statistical method is employed to calculate the Darcy velocity within a sufficiently large volume, surpassing the Representative Elementary Volume (REV) size [5]. However, to avoid additional errors in the Darcy velocity estimation [44] and to maintain consistency in length scale concepts [76], a modified approach is adopted. Instead of the conventional three-direction volume averaging, the averaging process is performed on the x-z plane spanning the entire domain. This choice is justifiable as the physical variables (pressure, velocity) are independent of x and z, and solely depend on the y-direction. This horizontal-plane-averaging technique offers several advantages, including the elimination of fluctuations and the revelation of dominant patterns without introducing additional errors.

[Fig. 2](#) displays the plane-averaged velocity profile along the y-axis for a porous structure with a medium cluster size and a porosity of 0.6. In the clean channel region, the velocity profile closely resembles that of Poiseuille flow, except for the presence of a non-zero velocity at the free-porous interface. Within the bulk porous medium, the fluid velocity matches the Darcy filtration velocity. However, near the free-porous interface, there exists a distinct narrow zone where the

fluid velocity significantly exceeds the Darcy filtration velocity. This observation highlights the presence of enhanced flow near the interface region.

In addition, a comparison has been conducted between the pore-scale simulation results and three classic models: the B-J model, the O-W model, and the B-W model. These models have been selected based on their wide usage and representation of three distinct classes of boundary conditions: velocity-jump conditions, stress-jump conditions, and conditions involving transition layers. While there exist other models, such as two-domain models incorporating both velocity-jump and stress-jump conditions [77] and other one-domain models [57,78], these models either exhibit forms similar to the selected models [53] or involve numerous complex parameters that are computationally infeasible to evaluate in intricate 3D structures. Each of these classic models incorporates a model parameter: α in the B-J model, β in the O-W model, and c in the B-W model. Previous studies have proposed various recommended values for these parameters, which are detailed in [Appendix C](#). For a porosity of 0.6, empirical values of $\alpha = 0.1$, $\beta = 1.0$, and $c = 1.0$ have been suggested based on previous investigations [13, 30,79,80].

The results demonstrate significant disparities between both the B-J model (represented by open triangles) and the O-W model (represented by open diamonds) when compared to the pore-scale simulation results (represented by solid circles). While the B-W model agrees well with the simulation results in the clear channel and bulk porous medium, it fails to capture the flow characteristics within the narrow transition zone near the interface. Conversely, the O-W model, the only model that somewhat reflects the decreasing trend within this transition zone, greatly overestimates the fluid velocity. This comparison highlights that velocity distribution profiles, commonly employed in previous studies, are inadequate for quantifying flow in coupled systems. Firstly, the results obtained from different structures cannot be directly compared, thereby raising the possibility of better model performance in alternative structures. More importantly, velocity distribution profiles fail to capture the flow behavior within the transition zone, where most models exhibit deficiencies. Furthermore, velocity profiles are insufficient in addressing pivotal questions, such as whether the stress (or velocity gradient) is continuous at the interface. Hence, velocity profiles alone are insufficient for characterizing interfacial flow behaviors, and additional physical and quantitative factors are required to compare the performance of models in complex porous structures.

This work presents four key factors as follows to characterize the flow behavior in a coupled system quantitatively and to assess the performance of models at the free-porous interface.

- Slip velocity u_s . This slip velocity refers to the fluid velocity at the free-porous interface from the free-space side. This parameter essentially reflects the morphology of the porous structure at the interface by telling how much it differs from a solid wall. In the pore-scale simulations, this slip velocity can be obtained by interpolating the plane-averaged velocity profile for the intercept at the free-porous interface. Actually, except for the B-J model which admits a discontinuity of velocity, other models all suppose a continuous velocity at the interface, so that determination from either side of the interface shall provide the same result.
- Interface layer thickness δ . This parameter refers to the thickness of the interface region where the fluid velocity decays rapidly in the porous part. The existence of this region is the most important feature of this coupled system and this parameter describes how fast the fluid velocity decays inside this region. The thicker this interface layer, the more the interfacial flow deviates from Darcy flow in the bulk porous media. Inspired by the definition of the boundary layer, we here propose that the velocity of fluid inside this interface layer should meet the following inequality

$$u_s - u \leq 0.95 (u_s - u_{\text{Darcy}}), \quad (5)$$

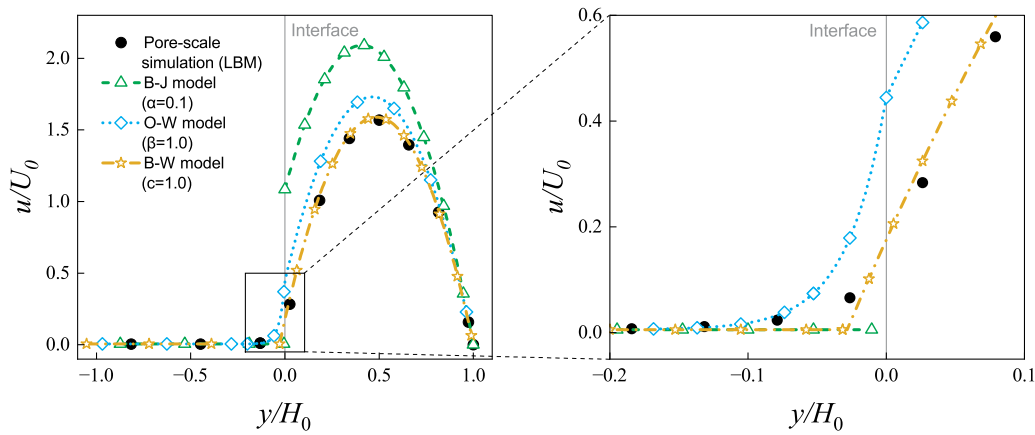


Fig. 2. Schematic diagram of the plane-averaged fluid velocity along the y -axis in a coupled system with a porous structure having a porosity of 0.6. The results of the pore-scale simulation and three previous models are shown in the left figure. The right figure provides an enlarged view of velocity profiles near the free-porous interface. U_0 and H_0 stand for the average velocity of Poiseuille flow and the height of the channel, respectively.

where u_{Darcy} is the Darcy filtration velocity and u_{slip} is the slip velocity. Since the Reynolds number in the system concerned in this work is much lower than that in the boundary layer theory, the deviation coefficient value of 0.99 may lead to a high numerical instability at the edge of the interface layer in the pore-scale simulation. A too-low value of this coefficient, such as 0.9, would cause this determined interface region to be unable to cover the entire transition region. Therefore a compromise value, 0.95, has been chosen to determine the thickness of this interface layer.

- Shear stress at the free-porous interface from the side of clean channel $\tau_{channel}$. The shear stress from the channel side reflects the magnitude of the force that the porous structure exerts on the outer flow. This value is calculated by

$$\tau_{channel} = \mu \left. \frac{\partial \langle u_\beta \rangle_\eta}{\partial y} \right|_{y \rightarrow 0^+} \quad (6)$$

In the pore-scale simulation, the velocity gradient on the right-hand side is calculated by extrapolation using the velocity of the neighboring three nodes in the clean channel.

- Shear stress difference between two sides at the free-porous interface τ_{dif} . The shear stress difference reflects the force balance at the interface. This value is determined by

$$\tau_{dif} = \tau_{channel} - \tau_{porous} = \mu \left. \frac{\partial \langle u_\beta \rangle_\eta}{\partial y} \right|_{y \rightarrow 0^+} - \mu_{eff} \left. \frac{\partial \langle u_\beta \rangle_\omega}{\partial y} \right|_{y \rightarrow 0^-}, \quad (7)$$

where $\mu_{eff} = \mu/\varepsilon$, following conventions from the previous studies [63,80–83]. A positive shear-stress difference means that the shear stress from the channel side is larger than that from the porous side, and vice versa. The two velocity gradients on the right-hand side are calculated using the same extrapolation method as stated above in the pore-scale simulation.

All four of these parameters possess clear physical interpretations and can be easily quantified. Among them, particular emphasis should be placed on the last two parameters, particularly the shear stress difference, as it directly reflects the consequences of fluid–solid interactions arising from the presence of porous structures.

A total of 48 random porous structures with diverse porosity and permeability values were chosen for analysis. Pore-scale simulations were conducted in the corresponding coupled flow systems to calculate the values of the four key factors mentioned above. The outcomes are presented in Fig. 3, where each data point represents an individual structure. Distinct sizes and colors indicate different cluster sizes. To determine the permeability (K) of the porous structures, supplementary pore-scale simulations were performed within these structures employing periodic boundary conditions.

In Fig. 3(a), it is observed that the slip velocity demonstrates a linear correlation with the square root of permeability. As permeability approaches zero, the slip velocity also tends to zero, indicating that the porous medium is equivalent to a solid wall. On the other hand, the interface layer thickness is proportional to the square root of permeability divided by porosity. The presence of stochastic factors in the structure generation process can lead to larger fluctuations in interface layer thickness for structures with higher porosity values. To obtain the precise location of the interface layer edge, interpolation methods were utilized due to the discretization in the pore-scale simulations, resulting in a small positive intercept. The fluid shear stress at the free-porous interface, originating from the channel side, exhibits a linear decrease with the square root of permeability. Notably, the intercept of the fitting line remains constant, equaling the velocity gradient at the solid wall in a planar Poiseuille flow with the same channel height and pressure gradient. As permeability increases, the flow in the free channel deviates further from Poiseuille flow. These three factors display strong linearity regardless of cluster sizes. It is possible for data points of different sizes and colors to overlap since structures with varying porosity and cluster sizes may occasionally possess similar permeabilities.

Fig. 3(d) illustrates the shear stress difference, which exhibits a non-linear relationship with permeability. As permeability approaches zero, the shear stress difference converges to a fixed value, corresponding to the scenario where the porous medium is replaced by a solid wall. With increasing permeability, the shear stress difference initially decreases rapidly and then gradually approaches zero, indicating the transition from the porous region to a clear channel. It is noteworthy that the shear stress difference remains positive regardless of the structure’s permeability, indicating that the fluid shear stress from the channel side is always greater than that from the porous side. Among the four key factors, the shear stress difference is the most sensitive to the interfacial morphology of the porous structure, leading to the zig-zag patterns observed in Fig. 3(d). Porous structures with similar permeabilities may possess different grain sizes, resulting in distinct surface morphologies and consequently yielding varying shear stress difference values.

The results of the three existing models are also presented in Fig. 3. The B-W model demonstrates favorable performance in predicting slip velocity, whereas both the B-J model and the O-W model with previously suggested parameter values exhibit significant overestimation in slip velocity. Conversely, only the O-W model exhibits good agreement with simulation results for the interface layer thickness, whereas the other two models underestimate this parameter. In terms of fluid shear stress from the channel side, only the B-W model shows satisfactory alignment with the pore-scale simulation, while the other two models underestimate this parameter. However, none of the three models

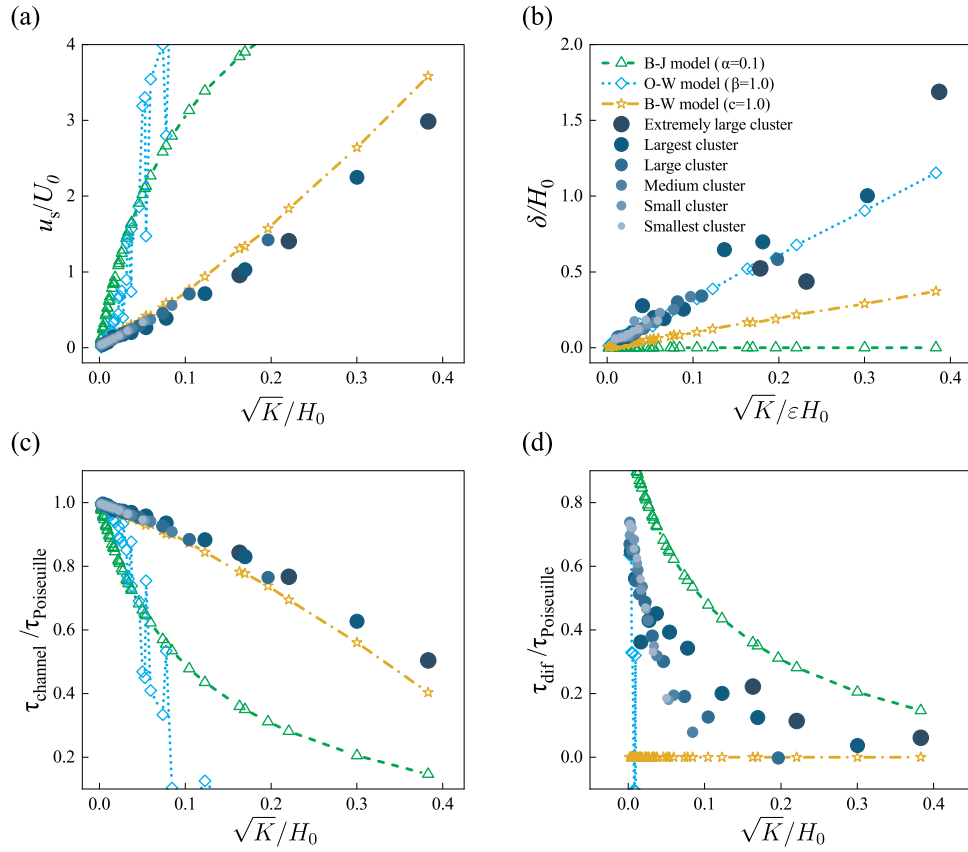


Fig. 3. Non-dimensional results of the four key factors by pore-scale simulations and three classic models of pressure-driven flow in coupled systems. (a) slip velocity. (b) interface layer thickness. (c) fluid shear stress on the channel side at the free-porous interface. (d) shear stress difference between two sides at the free-porous interface ($\tau_{\text{dif}} = \tau_{\text{channel}} - \tau_{\text{porous}}$). U_0 , H_0 , and $\tau_{\text{Poiseuille}}$ are the average velocity, the height of the channel, and the fluid shear stress at the wall in a corresponding Poiseuille flow, respectively.

provide satisfactory results for the shear stress difference. Among them, only the B-J model displays a similar decreasing trend, whereas the other two models yield incorrect predictions.

To examine the universality of the aforementioned relationships for the four key factors, shear-driven flows were simulated in the coupled flow systems consisting of a clean channel and the same 48 porous structures. In the shear-driven flow, the pressure gradient was set to zero, and a constant velocity was applied to the upper wall, approximately equal to the maximum velocity in the pressure-driven flow, ensuring a similar Reynolds number. All other conditions were kept consistent. The results of these simulations as well as the three classic models are presented in Fig. 4.

In the shear-driven flow, the same relationships persist for all four key factors. The linearity of the first three factors becomes even stronger, particularly for the interface layer thickness, as the filtration velocity in the bulk porous media is zero, resulting in reduced fluctuations. The results for the shear stress difference remain largely unchanged since the surface morphology of the porous structures remains the same.

The results of these models are consistent, as each model demonstrates satisfactory performance in one or two parameters while falling short in others. The B-J model exhibits a similar decreasing trend in shear stress difference compared to the pore-scale simulation. The O-W model yields satisfactory results for the interface layer thickness, while the B-W model performs well in predicting slip velocity and fluid shear stress from the channel side

These findings highlight the significant influence of the porous medium morphology in the free-porous coupled flow system, with permeability emerging as the dominant parameter. Notably, the square root of permeability, \sqrt{K} , appears to serve as a characteristic length scale in boundary flow problems involving porous media. The outcomes

obtained from the aforementioned classical models underscore their limitations in accurately capturing the dynamics of free-porous coupled flow systems that involve complex 3D porous structures, particularly in accurately representing the force balance at the free-porous interface.

4. Brinkman double-layer model

Based on the aforementioned limitations of previous macroscopic models in accurately representing the four key parameters in free-porous coupled flow systems, it is evident that these models fail to capture the underlying physical mechanisms. In this section, we introduce a novel model called the Brinkman double-layer (BDL) model to describe fluid flow in the coupled system. By incorporating the four key factors proposed in the previous section, we aim to validate this new model and compare its performance against pore-scale simulation results.

In this BDL model, the Stokes equation is used to describe flow in the clean channel. At the free-porous interface, an obvious velocity-continuum condition and a stress-jump condition are proposed corresponding to pore-scale simulation results:

$$\langle \mathbf{u}_\beta \rangle_\eta = \langle \mathbf{u}_\beta \rangle_\omega, \quad (8)$$

$$\frac{\partial \langle \mathbf{u}_\beta \rangle_\eta}{\partial y} - \frac{1}{\epsilon} \frac{\partial \langle \mathbf{u}_\beta \rangle_\omega}{\partial y} = (1 - \epsilon) \cdot \gamma \cdot \frac{\mathbf{u}_s}{\sqrt{K}}. \quad (9)$$

The detailed derivation of these boundary conditions is included in Appendix D for interested readers.

In the above and following equations, we use some notations that have been commonly adopted by studies employing the volume-averaging technique [62,65,84,85]: β refers to the fluid phase, σ refers

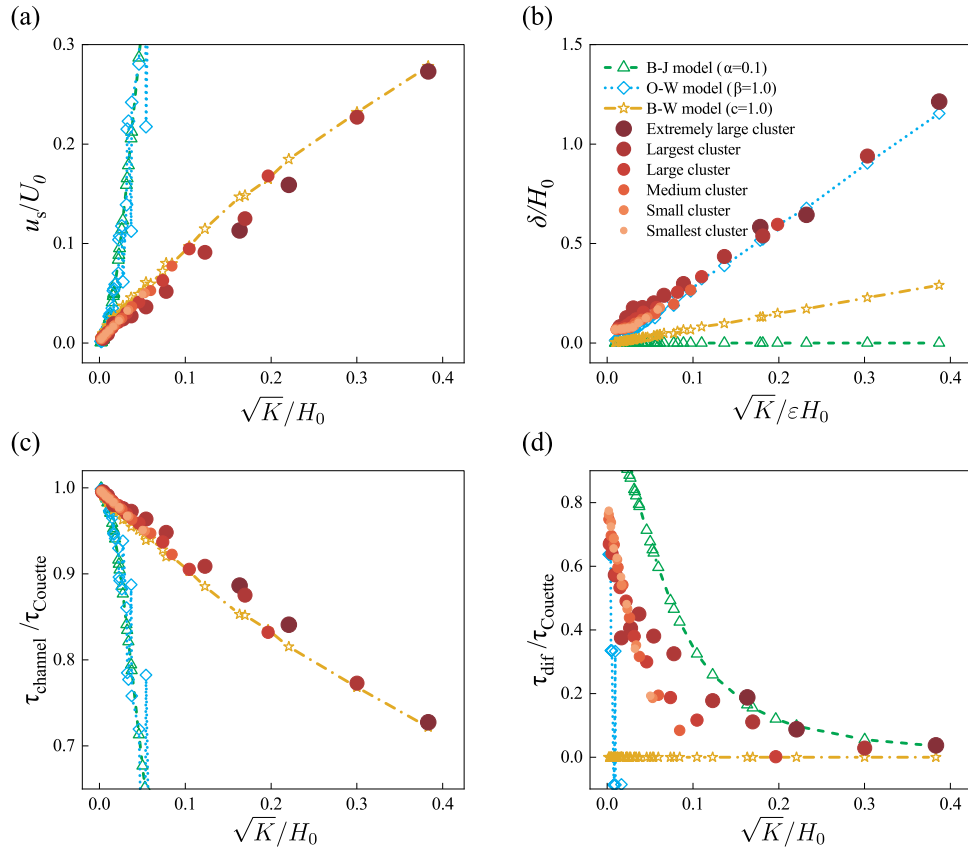


Fig. 4. Non-dimensional results of the four key factors by pore-scale simulations of shear-driven flow in coupled systems. (a) slip velocity. (b) interface layer thickness. (c) fluid shear stress on the channel side at the free-porous interface. (d) shear stress difference between two sides at the free-porous interface ($\tau_{\text{dif}} = \tau_{\text{channel}} - \tau_{\text{porous}}$). U_{wall} , H_0 , and τ_{Couette} stand for the velocity of the moving upper wall, the height of the channel, and the fluid shear stress in the corresponding Couette flow, respectively.

to the solid phase, ω refers to the porous medium, and η refers to the clean channel. We also introduce two definitions of average velocity: one is the intrinsic average velocity $\langle u_\beta \rangle^\beta$, and the other is the superficial average velocity $\langle u_\beta \rangle$. These two velocities are related by

$$\langle u_\beta \rangle^\beta = \frac{1}{\epsilon} \langle u_\beta \rangle, \quad (10)$$

in which ϵ stands for the porosity of the porous medium.

In the stress-jump condition, there is a dimensionless model parameter γ . It has been introduced in a linear assumption of the shear stress function f due to the linearity of the flow system:

$$f(\mathbf{u}_s, K, \epsilon) = \mu \cdot \gamma(\epsilon) \cdot \frac{\mathbf{u}_s}{\sqrt{K}}, \quad (11)$$

and is supposed to be a dimensionless constant related to the characteristics of the microstructures of the porous medium. By dimensional analysis, this γ should be a function of porosity ϵ , which will be studied later.

The linear Darcy equation is primarily a linear empirical equation applicable for characterizing flows in the bulk of porous media, rendering it inadequate for describing flow within the interface layer. Brinkman [86] introduced modifications to achieve a formulation of the equation that adheres to boundary conditions, resulting in what is commonly known as the Brinkman equation. This modified equation encompasses the Darcy term and an additional second-order differential term of velocity. The Brinkman equation is of second order and thus compatible with the Stokes equation. Neale and Nader [23] was the first to employ the Brinkman equation in describing flow within porous media in the free-porous coupled flow system. Nevertheless, certain experiments and simulations have highlighted discrepancies between the velocity profile depicted by the Brinkman equation and

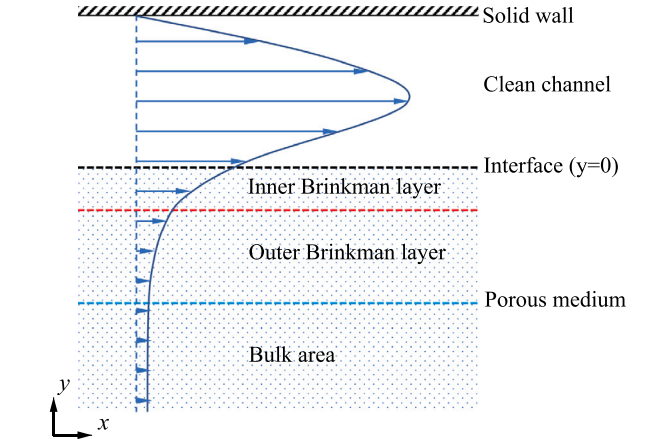


Fig. 5. A schematic diagram of the Brinkman double layers near the free-porous interface.

the observed behavior, often leading to overestimation of seepage velocities [32,39,43]. These findings suggest that a singular exponential curve from the Brinkman equation fails to entirely capture the velocity characteristics within the interface region. Consequently, the present study introduces a double-layer structure, named after Brinkman, as an alternative approach to elucidate fluid flow characteristics within the boundary region. (Fig. 5).

The inclusion of additional terms beyond the Darcy term in the interfacial region is necessitated by the need to achieve force equilibrium within porous structures in the presence of adjacent high-velocity outer

flow. Various forces come into play in this region, including bulk damping resistance arising from the porous structure, viscous resistance due to the no-slip boundary, viscous force exerted by the adjacent fluid, and pressure gradient (if a pressure difference exists) [28]. Consequently, this force balance evolves as the distance from the free-porous interface varies. Previous studies have highlighted that the applicability of the Brinkman term might be limited to the immediate vicinity of the free-porous interface [27], and a new term may be required to bridge the gap between the Brinkman and Darcy terms for fluid located further away from the interface within this interfacial region.

In the current model, the interfacial region within the porous medium is divided into two layers with distinct governing equations for each layer. The inner layer, referred to as the inner Brinkman layer (ω_1), is described by the Brinkman equation. Through dimensional analysis, it becomes evident that the influence of the outer flow diminishes as one goes deeper into the porous media, rendering the Brinkman term inapplicable beyond a certain depth. Consequently, in the outer layer, known as the outer Brinkman layer (ω_2), a first spatial derivative is introduced as a replacement for the Brinkman term. By comparing the second derivative term of velocity (associated with the Brinkman term) with this first derivative term, the following relationship can be established

$$\frac{\mu_\beta}{\varepsilon} \nabla^2 \langle \mathbf{u}_\beta \rangle_{\omega_1} \sim \frac{\mu_\beta}{\varepsilon \sqrt{K}} \nabla \langle \mathbf{u}_\beta \rangle_{\omega_2}. \quad (12)$$

This comparison leads to the conclusion that

$$y \sim \sqrt{K}, \quad (13)$$

indicating that the influence of the Brinkman term diminishes as the depth increases and is gradually replaced by the first derivative term. This relationship also suggests that the thickness of the inner Brinkman layer should be of the same order of magnitude as \sqrt{K} .

Similarly, the total thickness of the Brinkman layer, comprising both the inner and outer Brinkman layers, can be estimated using the following comparison:

$$\frac{\mu_\beta}{\varepsilon \sqrt{K}} \nabla \langle \mathbf{u}_\beta \rangle_{\omega_2} \sim \frac{\mu_\beta}{K} \langle \mathbf{u}_\beta \rangle_{\text{Bulk}}. \quad (14)$$

This yields the relationship:

$$y \sim \sqrt{K}/\varepsilon, \quad (15)$$

indicating that the total thickness of the Brinkman layer should be of a comparable magnitude to \sqrt{K}/ε . This represents the boundary of the interface layer. Beyond this depth, the influence of the outer flow diminishes, and the seepage velocity approaches the Darcy velocity. This offers a good explanation of the strong linearity between interface layer thickness and the square root of the permeability over porosity, as obtained by previous pore-scale simulations.

Given the homogeneity of the porous structures and the continuity of both solid and fluid phases, it is expected that velocity, stress, and pressure remain continuous across the interface between the inner and outer Brinkman layers. Therefore, the pressure $\langle p_\beta \rangle^\beta$ should also exhibit continuity across this interface. For simplicity, we designate the location of this interface as $-\sqrt{K}$. It is worth noting that for more accurate results, this location could be chosen as $-c\sqrt{K}$, where c is an additional parameter that can be determined through fitting experiments or simulation results. However, the improvement gained from this refinement is minor compared to the increased complexity it introduces.

Thus, the complete mathematical description of the Brinkman double-layer model for the coupled flow system can be summarized by incorporating the governing equations and boundary conditions as follows:

B.C.1 (solid wall)

$$\mathbf{u} = 0, \quad \text{at } y = H, \quad (16)$$

in which H marks the height of the clean channel.

Eq. (1) (flow in the clean channel)

$$0 = -\nabla \langle p_\beta \rangle_\eta^\beta + \mu_\beta \nabla^2 \langle \mathbf{u}_\beta \rangle_\eta, \quad 0 < y < H. \quad (17)$$

B.C.2&3 (free-porous interface)

$$\langle \mathbf{u}_\beta \rangle_\eta = \langle \mathbf{u}_\beta \rangle_{\omega_1}, \quad \text{at } y = 0. \quad (18)$$

$$\frac{\partial \langle \mathbf{u}_\beta \rangle_\eta}{\partial y} - \frac{1}{\varepsilon} \frac{\partial \langle \mathbf{u}_\beta \rangle_{\omega_1}}{\partial y} = \gamma(1 - \varepsilon) \frac{\mathbf{u}_s}{\sqrt{K}}, \quad \text{at } y = 0. \quad (19)$$

Eq. (2) (inner Brinkman layer)

$$0 = -\nabla \langle p_\beta \rangle_{\omega_1}^\beta + \frac{\mu_\beta}{\varepsilon} \nabla^2 \langle \mathbf{u}_\beta \rangle_{\omega_1} - \frac{\mu_\beta}{K} \langle \mathbf{u}_\beta \rangle_{\omega_1}. \quad (20)$$

B.C.4&5 (interface between inner and outer Brinkman layer)

$$\langle \mathbf{u}_\beta \rangle_{\omega_1} = \langle \mathbf{u}_\beta \rangle_{\omega_2}, \quad \text{at } y = -\sqrt{K}, \quad (21)$$

$$\frac{\partial \langle \mathbf{u}_\beta \rangle_{\omega_1}}{\partial y} = \frac{\partial \langle \mathbf{u}_\beta \rangle_{\omega_2}}{\partial y}, \quad \text{at } y = -\sqrt{K}. \quad (22)$$

Eq. (3) (outer Brinkman layer)

$$0 = -\nabla \langle p_\beta \rangle_{\omega_2}^\beta + \frac{\mu_\beta}{\varepsilon \sqrt{K}} \nabla \langle \mathbf{u}_\beta \rangle_{\omega_2} \cdot \frac{\mathbf{u}_\beta}{|\mathbf{u}_\beta|} - \frac{\mu_\beta}{K} \langle \mathbf{u}_\beta \rangle_{\omega_2}. \quad (23)$$

B.C.6 (flow in the bulk of porous medium)

$$\langle \mathbf{u}_\beta \rangle_{\omega_2} \rightarrow \mathbf{u}_{\text{Darcy}}, \quad \text{when } y \rightarrow -\infty. \quad (24)$$

By solving Eqs. (16) ~ (24), the velocity field and pressure/stress field can be obtained. One notable advantage of this model is its ability to yield simple analytical solutions for unidirectional flows. The analytical solutions for pressure-driven flow are presented below:

$$u_\eta(y) = \frac{\nabla p}{\mu} (y - H)(y/2 + C_1 \sqrt{K}), \quad 0 < y \leq H, \quad (25)$$

$$u_{\omega_1}(y) = -\frac{K \nabla p}{\mu} (1 + C_2 e^{\sqrt{\varepsilon/K} y} + C_3 e^{-\sqrt{\varepsilon/K} y}), \quad -\sqrt{K} \leq y < 0, \quad (26)$$

$$u_{\omega_2}(y) = -\frac{K \nabla p}{\mu} (1 + C_4 e^{\varepsilon y / \sqrt{K}}), \quad y < -\sqrt{K}, \quad (27)$$

where

$$C_1 = \frac{\sqrt{K}(1 + C_2 + C_3)}{H}, \quad (28)$$

$$C_2 = \frac{\sigma/2 - 1/\sigma - \gamma(1 - \varepsilon)}{[1/\sigma + 1/\sqrt{\varepsilon} + \gamma(1 - \varepsilon)] + [1/\sigma - 1/\sqrt{\varepsilon} + \gamma(1 - \varepsilon)] \cdot \frac{1 - \sqrt{\varepsilon}}{1 + \sqrt{\varepsilon}} \cdot e^{-2\sqrt{\varepsilon}}}, \quad (29)$$

$$C_3 = C_2 \cdot \frac{1 - \sqrt{\varepsilon}}{1 + \sqrt{\varepsilon}} \cdot e^{-2\sqrt{\varepsilon}}, \quad (30)$$

$$C_4 = (C_2 e^{-\sqrt{\varepsilon}} + C_3 e^{\sqrt{\varepsilon}}) \cdot e^\varepsilon. \quad (31)$$

4.1. Determination of γ

The coefficient γ has been supposed to be a dimensionless coefficient related to the structural characteristics of the porous medium. The pressure-jump condition Eq. (9) can be rewritten as:

$$\gamma = \frac{\frac{\partial \langle \mathbf{u}_\beta \rangle_\eta}{\partial y} - \frac{1}{\varepsilon} \frac{\partial \langle \mathbf{u}_\beta \rangle_\omega}{\partial y}}{(1 - \varepsilon) \frac{\mathbf{u}_s}{\sqrt{K}}}. \quad (32)$$

To estimate the value of γ for each porous structure, all the terms on the right-hand side of the equation can be calculated through pore-scale simulations. This allows for the determination of γ based on the specific structural properties of the porous medium under investigation.

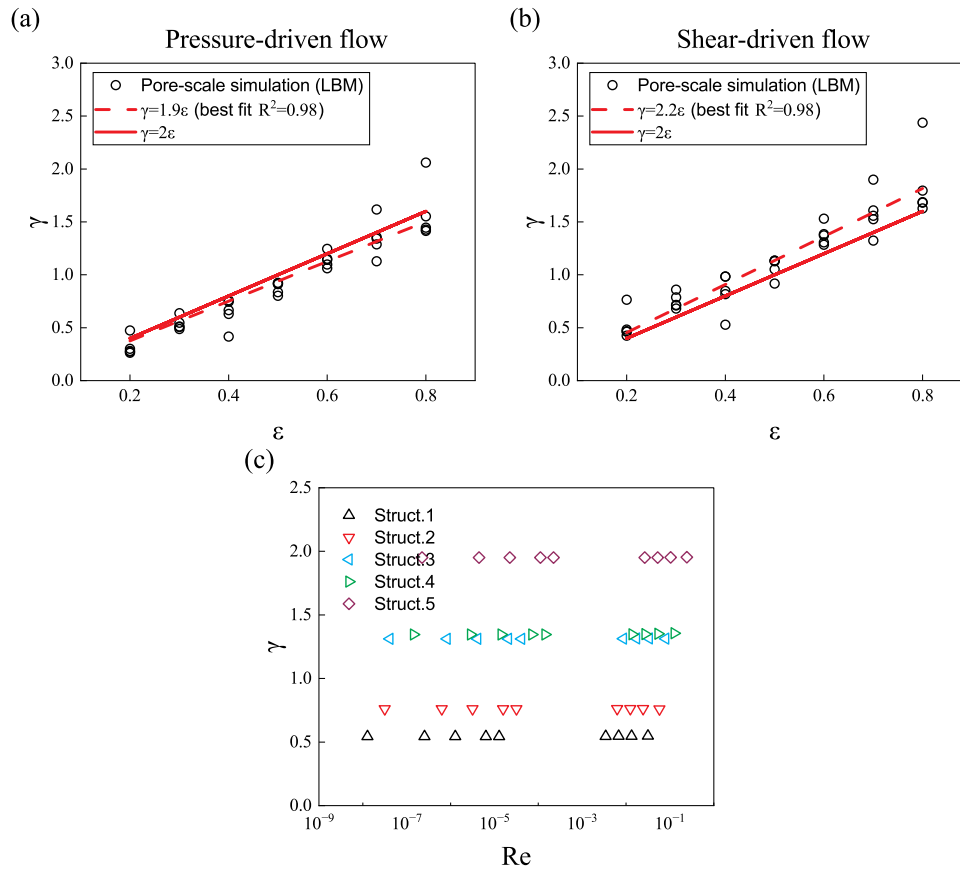


Fig. 6. Relationship between the dimensionless coefficient γ and (a) porosity ϵ in pressure-driven flow, (b) porosity ϵ in shear-driven flow, and (c) Reynolds number in pressure-driven flow. At each value of porosity in (a) and (b), structures with five different grain sizes were tested. The Darcy filtration velocity and average pore size are chosen as the characteristic velocity and length in calculating the Reynolds number.

The obtained values of γ in both pressure-driven and shear-driven flows are then analyzed, as presented in Fig. 6. Structures with porosities exceeding 0.9 are excluded from the analysis due to the presence of sporadically distributed solid grains that are not characteristic of natural porous structures. Nonetheless, the results obtained for these structures still adhere to the linear relationship discussed below, albeit with increased scattering.

The discovered linear relationships between γ and porosity for porous structures of varying porosity levels reveal interesting insights. In the case of pressure-driven flow, a linear fit with zero intercept yields $\gamma = 1.9\epsilon$, while for shear-driven flow, the linear fit results in $\gamma = 2.2\epsilon$. Both fits exhibit high correlation coefficients of 0.98. However, it is expected that the value of γ remains consistent and dependent solely on structural characteristics, irrespective of the flow driving mechanism.

In addition, the introduction of stochastic factors during the generation process of porous structures can lead to slight variations in the fitting values. To ensure consistency, elegance, and simplicity in practical applications, we propose a correlation formula that establishes a direct relationship between the model coefficient γ and the structural characteristics of the present Brinkman double-layer (BDL) model:

$$\gamma = 2\epsilon. \quad (33)$$

This correlation formula serves to bridge the gap between the model coefficient γ and the structural characteristics of the porous medium within the BDL model. The predictions generated by this simplified relation are represented by solid lines in Fig. 6(a) and (b), where they are compared against the results of pore-scale simulations and the best-fitting relationships. The agreement between the proposed simple correlation and the pore-scale modeling results is deemed acceptable based on both figures. Nonetheless, further verification is required to

Table 1

The value of porosity, cluster size, and permeability of the porous structures in the five selected coupled systems.

Name	Porosity	Cluster size	Permeability (D or 10^{-12} m ²)
Struct.1	0.2	Largest	0.22
Struct.2	0.4	Large	1.21
Struct.3	0.6	Small	3.62
Struct.4	0.6	Large	6.26
Struct.5	0.8	Medium	18.44

determine the universality of this linear relation in other specific types of porous media, such as fibrous porous structures. Nevertheless, this correlation can provide valuable guidance for applications involving common granular porous materials.

To investigate the influence of the Reynolds number on γ , further examinations were conducted. The Reynolds number of flow in the coupled systems was defined as $Re = \frac{u_D L}{\nu}$, where u_D represents the Darcy velocity in the bulk porous medium, L denotes the average pore size of the porous structure determined through the maximum ball method [69], and ν represents the fluid viscosity. The Reynolds number was manipulated by varying the pressure gradient in the pressure-driven flow. In order to provide clarity, the results of five representative structures were selected from the overall range of structures, and their properties are presented in Table 1. These structures likely exhibit different porosity and permeability values, which enable the exploration of a wide range of flow conditions. The obtained results are depicted in Fig. 6(c).

The findings indicate that when $Re \ll 1$, the value of γ remains unaffected by the Reynolds number. Additionally, pore-scale simulations were performed for the same structures under conditions where $Re \sim 1$.

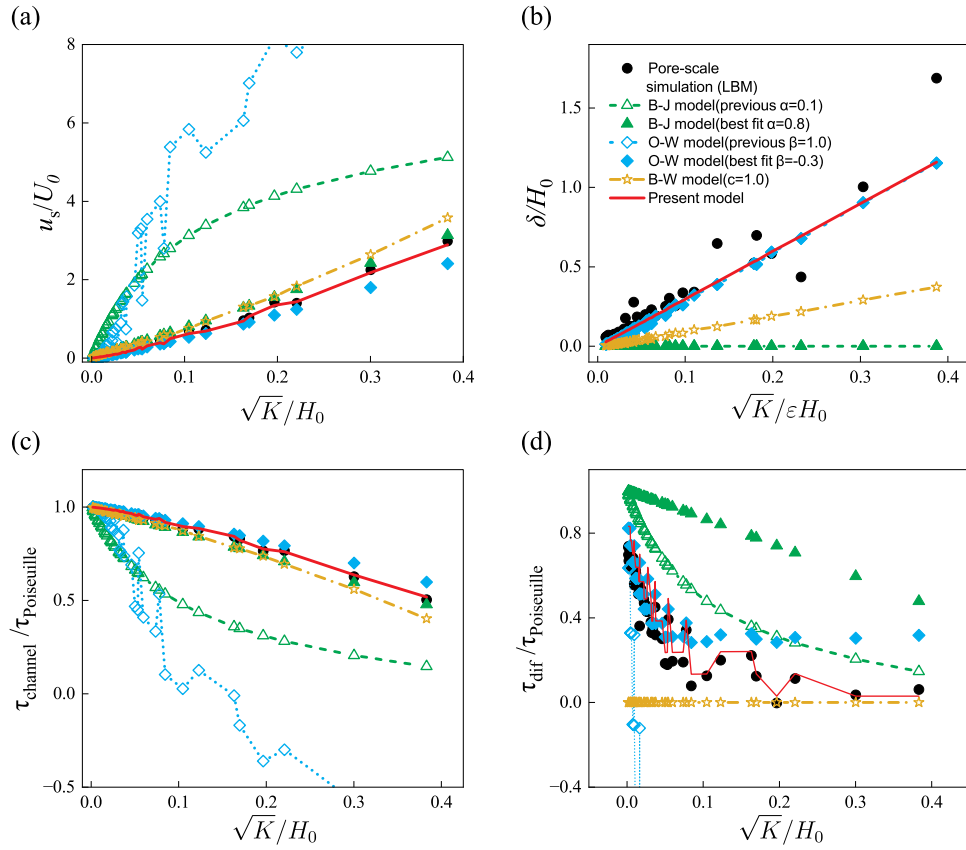


Fig. 7. Comparison of four key factors calculated by pore-scale simulations and different models in pressure-driven flows. (a) slip velocity. (b) thickness of the interface layer. (c) fluid shear stress on the channel side at the free-porous interface. (d) shear stress difference between two sides at the free-porous interface.

As depicted in Fig. 6(c), even at significantly larger Reynolds numbers, the parameter γ displays minimal differences compared to the low Re cases. It is worth noticing that when the Reynolds number defined above approaches one, the Reynolds number defined by using channel height H as the characteristic length has already exceeded one. Since the LBM scheme can fully recover the N-S equation in the clean channel and the pore spaces in the porous media, this observation suggests that the present model may still exhibit reliable performance beyond the Stokes limit, as long as the channel flow stays in a laminar regime. Further investigations may be conducted concerning turbulent flow in the future.

This observation suggests that the present model may still exhibit reliable performance beyond the Stokes limit, as long as the Reynolds number does not exceed a certain threshold.

4.2. Comparison of different models

The performance of four models, namely the B-J model, the O-W model, the B-W model, and the proposed BDL model with the linear formula $\gamma = 2\varepsilon$, was compared to pore-scale simulation results based on the four key factors mentioned earlier. To highlight the advantages of the BDL model, modifications were made to the B-J model and the O-W model by fitting the slip velocity results. The modified values for α and β were determined as 0.8 and -0.3 , respectively. It should be noted that while values close to 0.8 have been used as reference values for α in some literature (albeit with different porosity or in different types of porous structures), the value of -0.3 , to the best of our knowledge, has never been reported in previous studies. In fact, according to previous investigations, β should have a positive value [63,80]. The value of -0.3 has no physical basis and was solely used for comparison purposes as a result of best-fitting.

Results of all four models with different model parameter values are compared to pore-scale simulation results for pressure-driven flow in the free-porous coupled systems, as shown in Fig. 7.

The slip velocity analysis revealed that both the B-J model and the O-W model with their previously suggested parameter values exhibit significant deviations from the simulation results. However, by using best-fitted model parameters, the agreement between these models and the simulation results improves to a great extent. Nonetheless, among all the models considered, the proposed BDL model demonstrates the best agreement with the simulation results. Regarding the interface layer thickness, both the present BDL model and the O-W model yield equally satisfactory results, while the other models fail to capture the correct behavior regardless of the chosen model parameters. In terms of the fluid shear stress from the channel side, the B-J model with modified parameters, the O-W model with modified parameters, the B-W model, and the BDL model all provide reasonably good results. However, the BDL model exhibits the best agreement with the simulation results. When examining the shear stress difference as the last factor, the BDL model stands out as the only model that consistently agrees well with the simulation results across all permeability values. In contrast, the B-J model, regardless of the chosen model parameters, exhibits significant deviations from the simulation results. The B-W model, which assumes stress continuity across the free-porous interface, yields trivial results. Although the O-W model with the modified β value agrees well with low-permeability structures, it fails to accurately predict the shear stress difference in high-permeability situations. The BDL model, on the other hand, not only captures the correct trend of shear stress difference with respect to permeability but also distinguishes structures with similar permeabilities but different microstructures, producing distinct zig-zag patterns.

The performance of the models was also evaluated for shear-driven flow in the free-porous coupled system using the same porous structures and model parameters as in the pressure-driven flow case. The

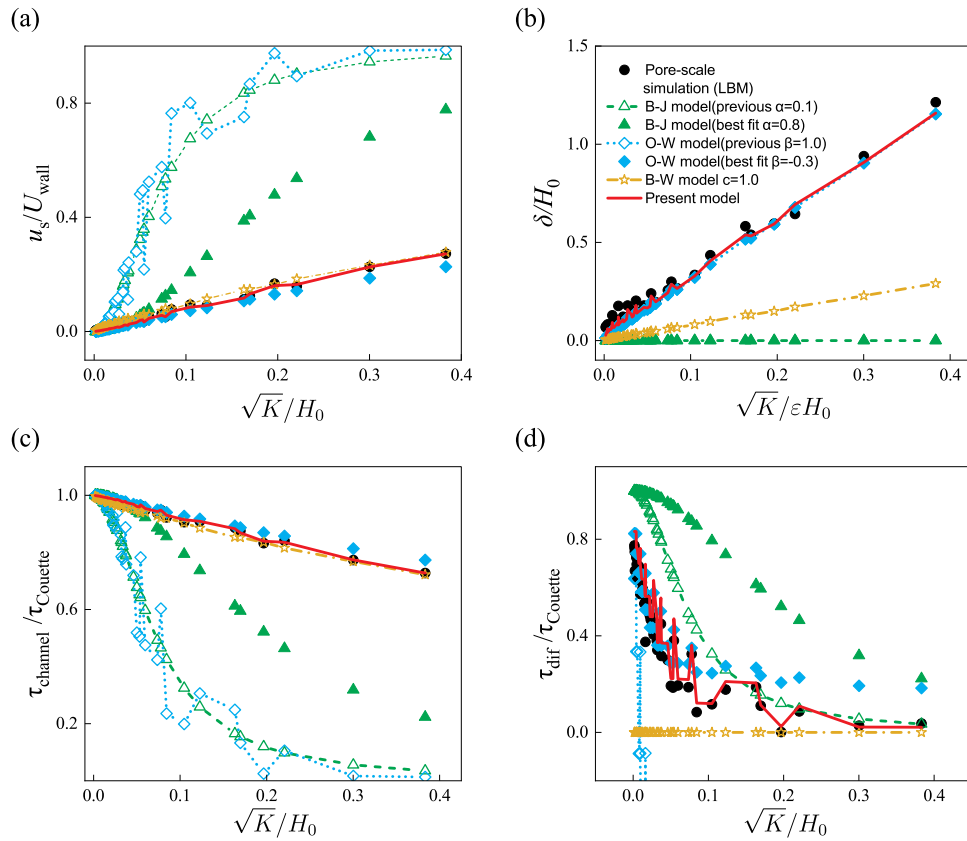


Fig. 8. Comparison of pore-scale simulation results with the different models in shear-driven flow. (a) slip velocity, (b) thicknesses of the interface layers, (c) fluid shear stress on the channel side at the free-porous interface, and (d) shear stress difference between two sides at the free-porous interface.

results, as shown in Fig. 8, exhibit similar trends to those observed in pressure-driven flow.

Notably, the B-J model with the modified α value fails to accurately predict all four key factors, resulting in non-linear trends in both the slip velocity and the fluid shear stress from the channel side. The B-W model performs slightly better in terms of the slip velocity and the fluid shear stress from the channel side, but it still falls short in accurately predicting the interface layer thickness and the shear stress difference. The O-W model with the modified β value yields good results for most factors except for the shear stress difference. In contrast, the BDL model consistently outperforms the other models, providing satisfactory results for all four key factors, particularly excelling in predicting the shear stress difference. These findings highlight the BDL model's ability to accurately capture the force balance and momentum transfer at the free-porous interface.

In summary, the BDL model demonstrates superior performance compared to the other models considered, including the B-J model, the O-W model, and the B-W model, for both pressure-driven and shear-driven flow in terms of slip velocity, interface layer thickness, fluid shear stress from the channel side, and shear stress difference. Its ability to provide a comprehensive and accurate representation of the complex flow behavior in porous media makes it a valuable tool for practical applications.

4.3. Comparison with previous experimental data

To further validate our model, we conducted a comparative analysis between the BDL model and experimental data reported by Wu and Mirbod [87] in 2018. In these experiments, porous media with intricate 3D random structures were utilized, resulting in stable, non-fluctuating velocity profiles that facilitate direct comparisons. In the following

comparisons, the model parameter γ was consistently defined as $\gamma = 2\epsilon$ for consistency and clarity.

Fig. 9 presents the results obtained across three distinct porous structures characterized by varying porosities. The solid line in the figure represents the predictions of the BDL model, while different point shapes correspond to experimental data obtained from different porous structures. We normalize both the fluid velocity and the y-coordinate by the channel height (H) and the maximum velocity, respectively.

Across all three structures, the BDL model demonstrates remarkable agreement with the experimental results. Notably, it excels in accurately predicting the slip velocity and capturing the trend of descending velocity within the thin interface layer. It is worth emphasizing that the porous structures investigated in these experiments exhibit significant differences from the granular structures examined in our study, underscoring the potentially broad applicability of our BDL model.

4.4. Sensitivity analysis on γ

The sensitivity of model parameters is a critical aspect to consider in any theoretical model. A model is deemed robust if minor adjustments to its parameters do not significantly alter its predictions. In the case of the BDL model, it is important to evaluate the sensitivity of the model to the parameter γ . To assess this sensitivity, different values ranging from 0 to 8 have been assigned to γ , and the corresponding predictions by the BDL model are compared with pore-scale simulation results in Fig. 10.

The comparisons demonstrate that even with a more than 400% increase in γ , the BDL model still exhibits good agreement with pore-scale simulation results for the slip velocity, interface layer thickness, and fluid shear stress from the channel side, as shown in Fig. 10. Although the shear stress difference between the two sides is slightly more sensitive to the value of γ (as depicted in Fig. 10(d)), the overall

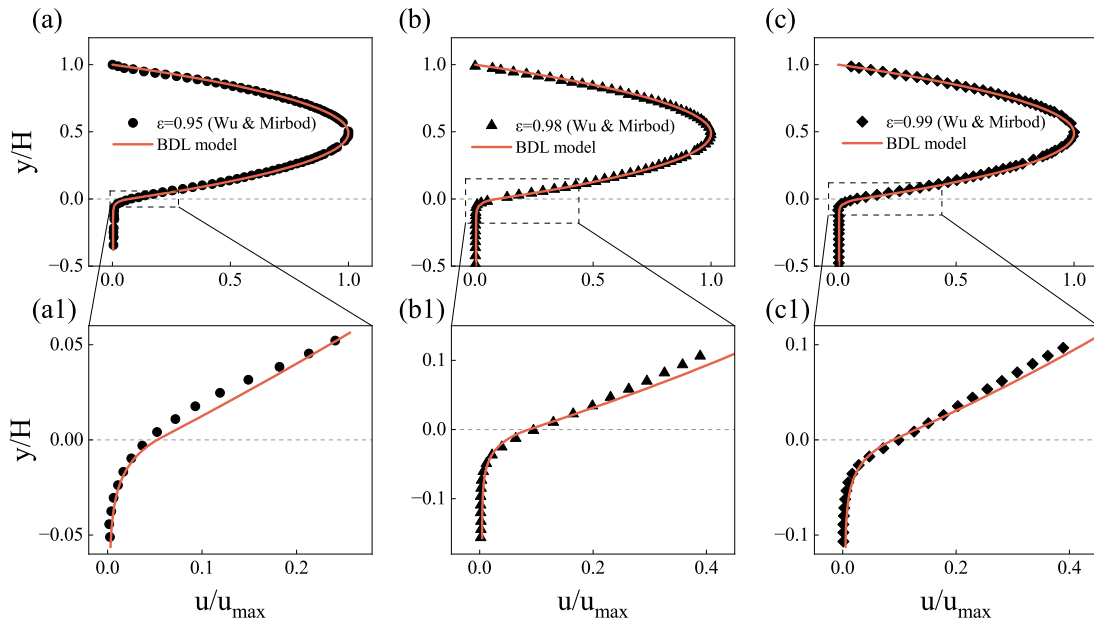


Fig. 9. Comparison between the BDL model and the experimental results by Wu and Mirbod [87]. (a) velocity profiles in the structure with a porosity of 0.95. (b) velocity profiles in the structure with a porosity of 0.98. (c) velocity profiles in the structure with a porosity of 0.99. (a1), (b1), and (c1) are corresponding local velocity profiles near the fluid-porous interface for the three structures. The interface is located at $y = 0$.

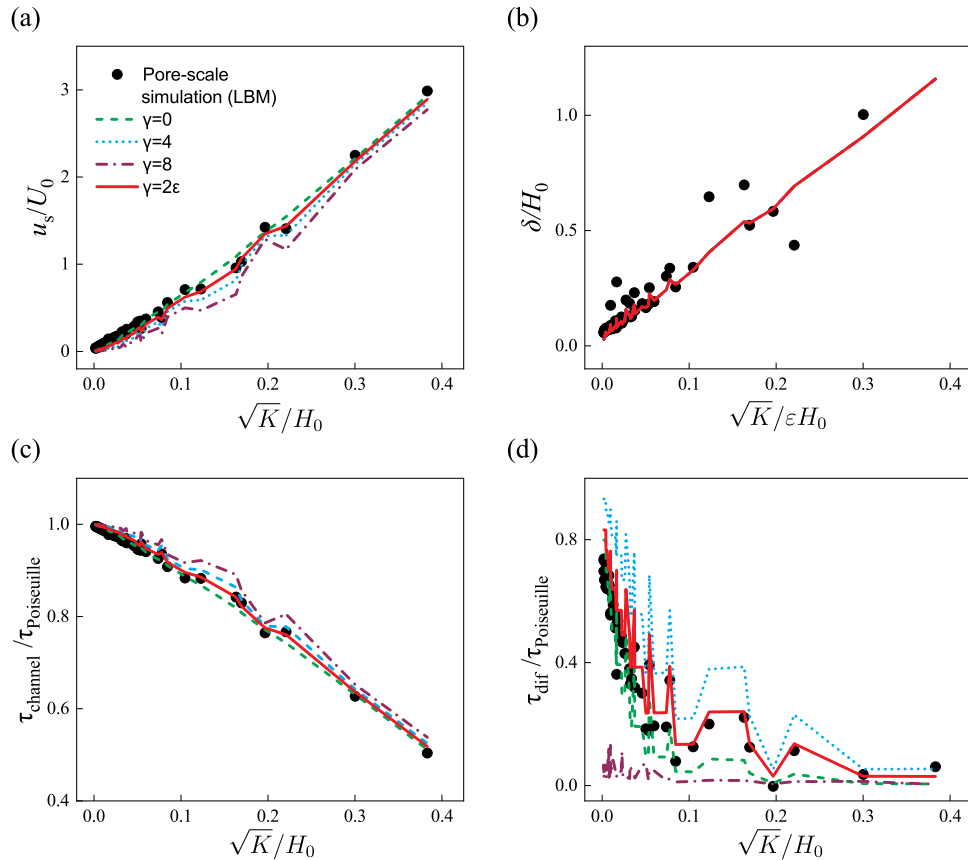


Fig. 10. Comparisons of the results of pore-scale simulation and the present model with different values of γ in pressure-driven flow. (a) shows the non-dimensional slip velocity v.s. permeability; (b) shows the non-dimensional interface layer thicknesses v.s. permeability; (c) shows the non-dimensional fluid shear stress on the channel side at the free-porous interface; and (d) shows the shear stress difference between two sides at the free-porous interface.

trend is still accurately captured for all cases. Therefore, the present BDL model demonstrates robustness to variations in the value of the model parameter γ within the range of $0 < \gamma < 6$.

In summary, the present BDL model not only improves the accuracy of predictions and establishes a physical correlation for the model parameter γ , but it also exhibits robust performance suitable

for engineering applications. The model's ability to maintain consistent results across a reasonable range of parameter values further enhances its practical utility.

5. Conclusions

In this study, we have provided comprehensive numerical investigations and modeling of flow in a coupled system consisting of a straight channel and a porous medium. Through the generation of realistic porous microstructures using the QSGS method and pore-scale fluid flow simulations using Lattice Boltzmann Method (LBM), we have gained valuable insights into the complex flow behavior near the free-porous interface.

By introducing four key parameters – slip velocity, interface layer thickness, fluid shear stress from the channel side, and fluid shear stress difference at the free-porous interface – we have successfully quantified and characterized the flow characteristics in the coupled system. Notably, linear relationships have been established between certain parameters and the square root of permeability, highlighting the significance of this quantity as a characteristic length in boundary flow problems involving porous media. The positive fluid shear stress difference across the interface consistently demonstrates a stress-jump condition, indicating a strong force balance and momentum transfer at the interface. Several existing models have been assessed by these four key parameters and their deficiencies have been illustrated.

To address the limitations of existing models, we have proposed the Brinkman double-layer (BDL) model, which incorporates a velocity-continuum interface condition, a new stress-jump interface condition, and a novel double-layer structure in the porous medium near the interface. The BDL model has demonstrated superior performance compared to three classic models, exhibiting excellent agreement with pore-scale simulation results across all four key parameters, particularly the shear stress difference at the free-porous interface. Furthermore, the BDL model has exhibited remarkable robustness, maintaining accurate predictions even with significant variations in the model parameter γ .

In summary, the BDL model offers a valuable tool for accurately representing and understanding the complex flow behavior in coupled systems comprised of channels and porous media. Its simplicity, accuracy, and robustness make it a promising candidate for a wide range of practical applications. Future research can focus on exploring the applicability of the BDL model to other types of porous media and validating its effectiveness in different flow regimes.

Funding

This work is funded by the National Key R&D Program of China (No. 2019YFA0708704), NSF grant of China (No. 12272207, U1837602) and the Tsinghua University Initiative Scientific Research Program, China for financial support.

CRediT authorship contribution statement

Jinliang Kang: Investigation, Software, Validation, Investigation, Writing – original draft. **Moran Wang:** Conceptualization, Supervision, Writing – reviewing & editing, Project administration.

Declaration of competing interest

The authors declare that they have no known competing financial interests or personal relationships that could have appeared to influence the work reported in this paper.

Data availability

No data was used for the research described in the article

Appendix A. QSGS algorithm and microstructure generations

The Quartet Structure Generation Set (QSGS) method has been developed as a reliable approach for generating complex microstructures of porous media within the coupled system. The QSGS utilizes statistical information, including porosity, grain size, and degree of isotropy, to randomly reproduce microstructures that closely resemble real or targeted porous media. The generation process consists of two main stages: seeding and growing, which closely mimic the natural formation process observed in many porous media.

During the seeding process, solid cores are randomly distributed throughout the entire domain. The number of solid cores is adjusted according to the desired grain size, with fewer cores for larger grains and vice versa. In the subsequent growing process, each solid core undergoes growth in all directions with a predefined probability. By manipulating the growth rate in different directions, the degree of isotropy in the resulting porous structure can be controlled. For our study, all generated porous structures are isotropic, with equal growth rates assigned to the six main directions. The growing process concludes when the porosity of the structure reaches or exceeds the desired value.

To measure the pore size distributions within the generated porous media, we employ the maximum ball method, as outlined by Gostick et al. [69]. Typically, the probability density function exhibits patterns similar to the Gaussian function, capturing the statistical characteristics of the microstructure. To ensure reliable simulation results, the size of the generated porous structures is set to be significantly larger than the average pore size.

In the context of generating porous structures within a cubic domain, we address the issue of non-uniform porosity near the edges of the structure, which arises due to boundary effects. To mitigate this concern, we apply a periodic boundary condition during the generation process of QSGS (Fig. A.11). The modified QSGS method ensures that the newly generated structures exhibit uniform porosity throughout. This approach enhances the accuracy of simulations and subsequent analyses.

Throughout this study, all porous structures have been generated using the modified QSGS method, guaranteeing a uniform porosity distribution for our mechanistic investigation. The advantages of this modified approach ensure reliable and consistent porosity profiles within the generated structures.

Appendix B. Validations of pore-scale modeling method

We validated the pore-scale modeling method, lattice Boltzmann method with single-relaxation-time (SRT) scheme or multiple-relaxation-time (MRT) scheme in this work, by simulating a Poiseuille flow in a 3D square channel with a constant pressure gradient. The analytical solution is as follows

$$u(x, y) = -\frac{\nabla p}{2\mu} \left[\frac{b^2}{4} - y^2 - C(x, y) \right], \quad (\text{B.1})$$

$$\text{with } C(x, y) = \frac{8b^2}{\pi^3} \sum_{n=0}^{\infty} (-1)^n \frac{\cosh((2n+1)\pi x/b) \cos((2n+1)\pi y/b)}{(2n+1)^3 \cosh((2n+1)\pi/2)}, \quad (\text{B.2})$$

where b stands for the side length of the square channel.

We conducted simulations with varying fluid viscosities in the square channel. The velocity profiles at the central plane were non-dimensionalized by the maximum velocity at the middle of the cross-section, and the results are presented in Fig. B.12(a). The results show excellent agreements between the analytical solution and pore-scale LBM simulations for different values of viscosity. To estimate the truncation error, we compared the simulation results obtained using

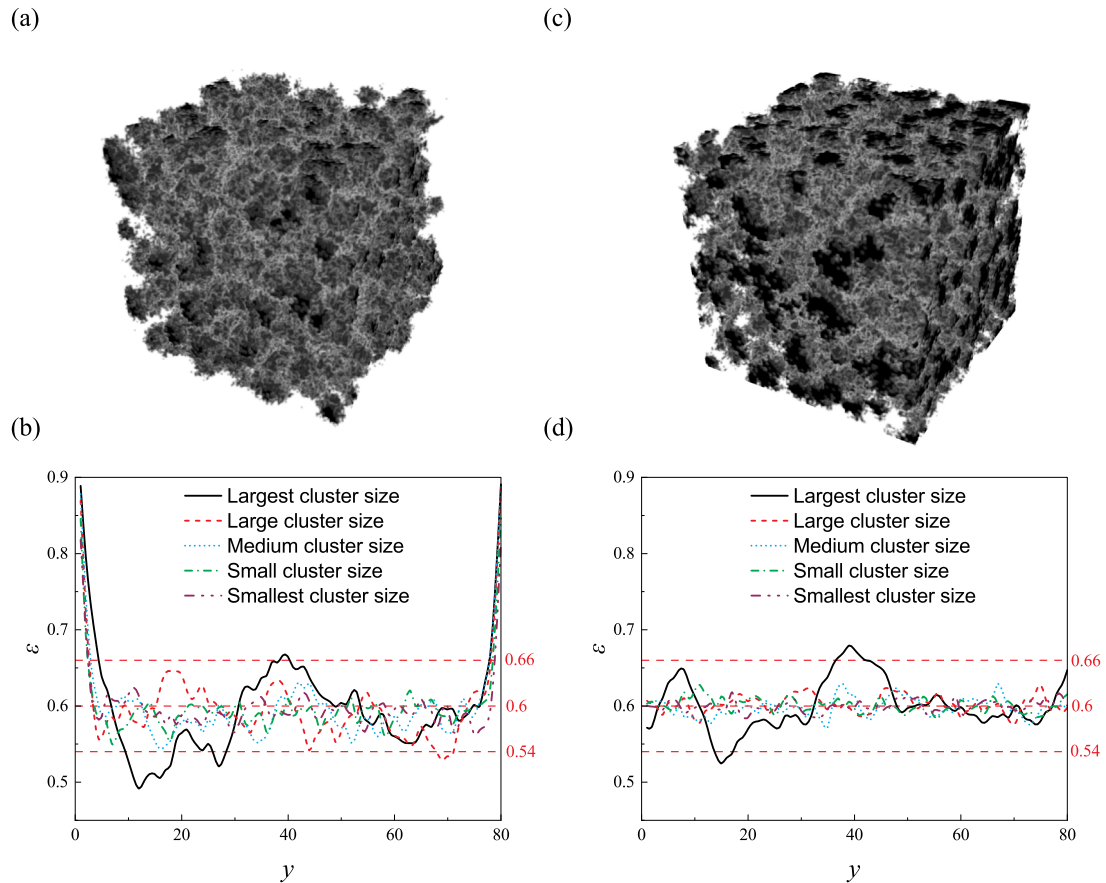


Fig. A.11. Schematic diagrams of generated porous structures by QSGS and the distribution of porosity. (a) microstructure generated under a constraint boundary, and (b) the corresponding porosity profiles for different grain sizes; (c) microstructure generated under a periodic boundary and (d) the corresponding porosity profiles for different grain sizes. The aiming porosity is 0.6 and the fluctuations using the periodic boundary condition are within 10% of the designed value.

different numbers of lattice points with the analytical solution and calculated the mean relative error of the velocity. For both the SRT and MRT schemes, the relative error decreases with the increase of lattice number, with slopes approximately equal to -2 (Fig. B.12b, c). The mean relative errors remain changeless for different values of fluid viscosity. The results indicate a second-order accuracy for both schemes of LBM.

To further validate our codes, we applied them to simulate flows in two classical spherical packing structures: the body-centered cubic (BCC) and the face-centered cubic (FCC) structures. Theoretical analysis demonstrates that the ratio of permeability over the square of sphere diameter is a constant for these two structures [88]. The constant value for FCC is 1.736×10^{-4} , while for BCC it is 5.023×10^{-4} . As the sphere diameter increases, the solid sphere surfaces become smoother due to lattice discretization in the pore-scale modeling, resulting in simulation results that approach the theoretical values. As depicted in Fig. B.13(a, b), the permeability calculated by LBM with an SRT scheme gradually approaches the theoretical value when the spheres grow for both BCC and FCC structures, consistent with findings in the literature [89]. The LBM simulation results obtained with the MRT scheme for these structures exhibit a similar trend across a wide range of fluid viscosities (Fig. B.13c, d).

The aforementioned results demonstrate the validity of our pore-scale algorithms and codes, enabling us to accurately simulate flow in complex porous structures with various fluid viscosities. This capability allows us to measure the permeability of generated porous structures, conduct simulations in the coupled system, and analyze flow behavior near the free-porous interface.

Appendix C. Selection of model parameters

The determination of empirical model parameters is an important aspect of previous models. Various studies have focused on finding suitable values for these dimensionless parameters. Among them, the value of α in the B-J model has garnered significant attention. The original study that developed the B-J model conducted quantitative experiments using foametal and aloxite, resulting in reference values of α ranging from 0.1 to 4.0, based on matching the total flow rate in the coupled system [13]. Subsequently, Beavers et al. [79] conducted experiments using foametal produced by GE and recommended a reference value of 0.1 for α . Other artificial materials, such as piles of cylinders [90] and networks of glass strands [42], have also been used, leading to different recommended values for α , most of which were below 1.

Early studies on the β parameter in the O-W model were carried out by Ochoa-Tapia and Whitaker [91], who used experimental data from [13] and proposed reference values around 0.6 for foametal structures and 1.47 for granular structures. In subsequent studies, different expressions for structure permeability were employed, resulting in different values for β . Most of these values were greater than one, such as 1.23 [63], 1.1, and 1.25 [80]. It is worth noting that in some previous works, researchers have formulated closure problems [80] to determine the parameter β . However, due to the complexity of the 3D porous structures generated in this study, solving these closure problems would incur a prohibitively high computational cost. Therefore, these approaches were not adopted in this work.

On the other hand, for the B-W model, the model parameter c has been suggested to have a reference value of 1.0, regardless of the structure type or porosity [30].

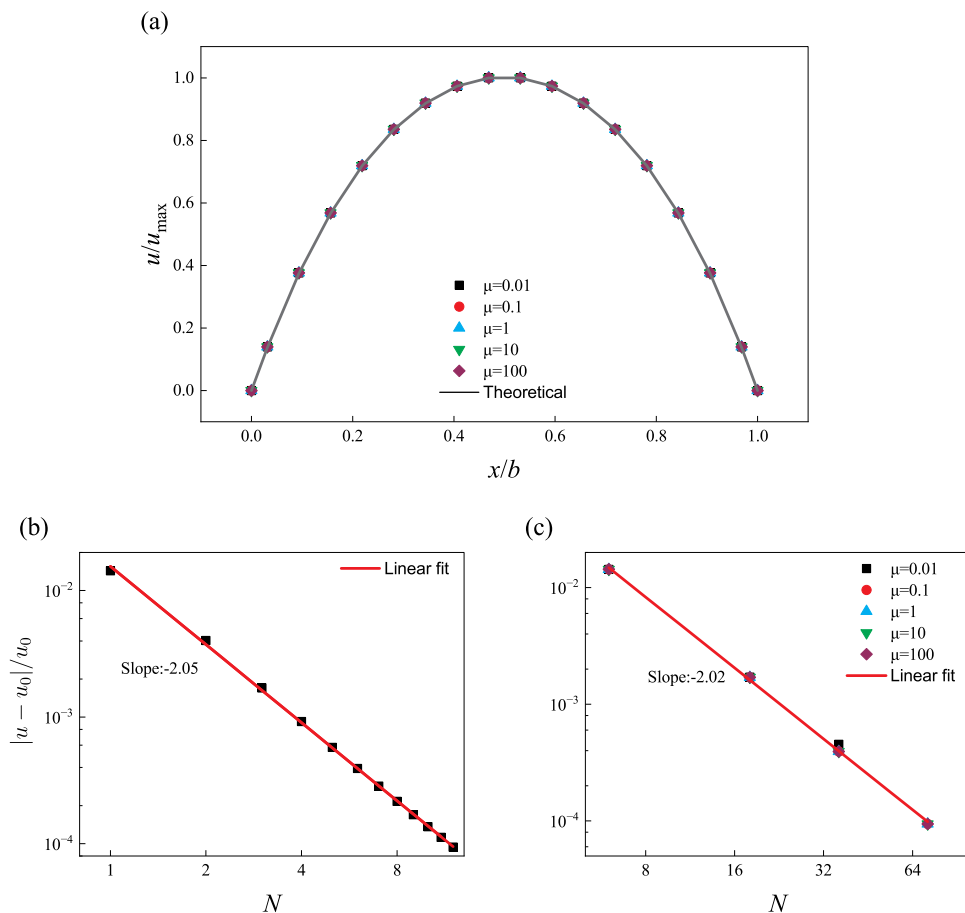


Fig. B.12. (a) shows the fluid velocity profile at the central plane parallel to the channel wall. u_{\max} and b stand for the maximum fluid speed at the central point of the cross-section and the side length of the square channel, respectively. Relative errors of the SRT LBM program and MRT LBM program with different fluid viscosity are shown in (b) and (c). N stands for the number of lattices per side of the square channel, and u_0 stands for the analytical solution.

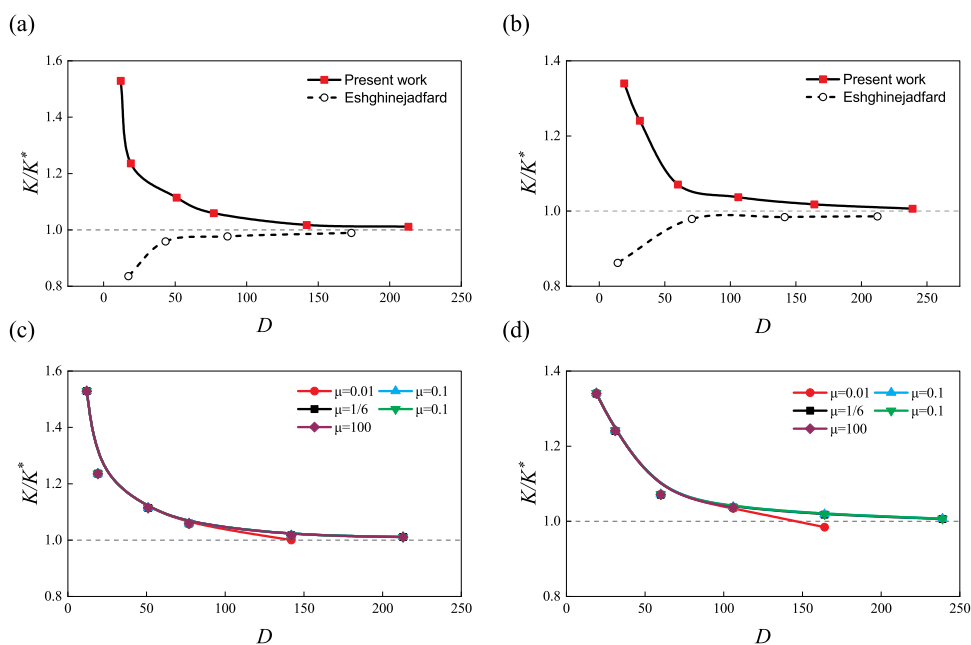


Fig. B.13. The permeability of BCC (a) and FCC (b) calculated by SRT-LBM used in this paper and a previous work by Eshghinejadfard et al. [89]. The permeability of BCC (c) and FCC (d) is calculated by our MRT-LBM with various values of fluid viscosity. K stands for the permeability calculated by LBM, K^* stands for the theoretical value, and D stands for the diameter of spheres in BCC and FCC structures.

Table C.2
Different values for the model parameters in previous models.

Model parameter	Model	Value	Porosity	Structure type	Reference
α	B-J model	0.78–4	0.8	Foametal	Beavers and Joseph [13]
α	B-J model	0.1	0.58	Granular	Beavers and Joseph [13]
α	B-J model	0.1	0.52	Granular	Beavers and Joseph [13]
α	B-J model	0.1	–	Foametal	Beavers et al. [79]
β	O-W model	1.47	0.58, 0.52	Granular	Ochoa-Tapia and Whitaker [91]
β	O-W model	1.23	–	Granular	Goyeau et al. [63]
β	O-W model	1.0	0.58	Granular	Valdés-Parada et al. [80]
c	B-W model	1.0	–	–	Bars and Worster [30]

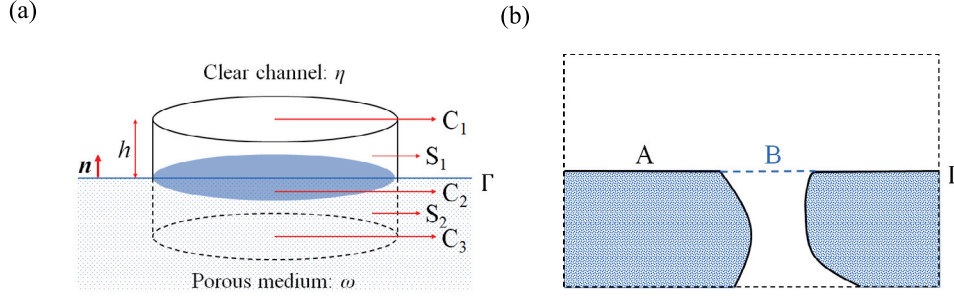


Fig. D.14. (a) Schematic of a cylindrical control volume across the free-porous interface. The volume is divided into two parts with the same height, h , by the interface Γ . (b) Schematic of the cuboid REV across the free-porous interface with only one pore plotted for clarity. Solid parts of the porous medium are denoted by the shaded area. A stands for the solid-liquid interface and B stands for the liquid-liquid interface.

The typical reference values for these parameters are summarized in Table C.2. Considering the structure type and porosity (e.g., the porosity of granular structures being around 0.6), we have chosen the model parameters that demonstrate the best performance for comparison. In this work, we selected $\alpha = 0.1$ and $\beta = 1.0$ as the reference values for the B-J model and the O-W model, respectively. For the parameter c in the B-W model, a value of 1.0 has been suggested irrespective of the structure type or porosity [30].

Appendix D. Derivation of Brinkman double-layer model

The volume-averaging method is employed to derive the boundary conditions at the interface. In the following sections, we use some notations that have been commonly adopted by studies employing the volume-averaging technique [62,65,84,85]: β refers to the fluid phase, σ refers to the solid phase, ω refers to the porous medium, and η refers to the clean channel. We also introduce two definitions of average velocity: one is the intrinsic average velocity $\langle \mathbf{u}_\beta \rangle^\beta$, and the other is the superficial average velocity $\langle \mathbf{u}_\beta \rangle$. These two velocities are related by

$$\langle \mathbf{u}_\beta \rangle^\beta = \frac{1}{\varepsilon} \langle \mathbf{u}_\beta \rangle, \quad (\text{D.1})$$

in which ε stands for the porosity of the porous medium.

A cylindrical control volume across the free-porous interface is selected to derive the velocity-continuum condition, as shown in Fig. D.14(a).

This volume V is separated into two parts by the interface Γ : the upper part V_η in the clean channel and the lower part V_ω in the porous medium. Since the fluid is assumed incompressible, one has the following continuity equation for pore-scale velocity

$$\nabla \cdot \mathbf{u}_\beta = 0. \quad (\text{D.2})$$

By the spatial averaging theorem [92], one can get the continuity equation for the average velocity

$$\nabla \cdot \langle \mathbf{u}_\beta \rangle = 0. \quad (\text{D.3})$$

Then, following the same deviations used by [54], one can derive the following equation

$$\langle \mathbf{u}_\beta \rangle_\eta = \langle \mathbf{u}_\beta \rangle_\omega, \quad \text{on } \Gamma. \quad (\text{D.4})$$

This shows that the averaged velocity is continuous across the interface Γ , which is natural and quite evident.

A cuboid representative elementary volume V across the interface is chosen to drive the stress-jump condition. Suppose the size of this volume is much larger than the pore size, but we only plot one pore for clarity (see Fig. D.14(b)). The free-porous interface included in the volume can be divided into two groups: the solid-liquid interface denoted by A and the liquid-liquid interface denoted by B . By analyzing the relationship of shear force at the interface, we have

$$\mu \frac{\partial \langle \mathbf{u}_\beta \rangle_\omega^\beta}{\partial y} - \mu \frac{\partial \langle \mathbf{u}_\beta \rangle_\eta^\beta}{\partial y} = 0, \quad \text{on } B, \quad (\text{D.5})$$

and assume

$$\tau_\eta = \mu \frac{\partial \langle \mathbf{u}_\beta \rangle_\eta^\beta}{\partial y} = \mathbf{f}, \quad \text{on } A. \quad (\text{D.6})$$

Here, \mathbf{f} is a function that should rely on the slip velocity u_s and the surface geometries of the porous structure. Since the porous medium is supposed to be homogeneous, this \mathbf{f} is then supposed to be a function of bulk porosity and permeability, which are the only two known geometrical parameters. Thus, \mathbf{f} is supposed to have the following form $\mathbf{f} = \mathbf{f}(u_s, K, \varepsilon)$.

Let $\varepsilon \times (2.8) - (1 - \varepsilon) \times (2.9)$, after simplification, we have

$$\left(\frac{\partial \langle \mathbf{u}_\beta \rangle_\omega^\beta}{\partial y} \right)_B - \frac{1}{\varepsilon} \frac{\partial \langle \mathbf{u}_\beta \rangle_\eta}{\partial y} = \frac{\varepsilon - 1}{\varepsilon} \cdot \frac{1}{\mu} \mathbf{f}(u_s, K, \varepsilon). \quad (\text{D.7})$$

Since the porous medium is supposed to be homogeneous, we have

$$\begin{aligned} \frac{\partial \langle \mathbf{u}_\beta \rangle_\omega}{\partial y} &= \varepsilon \left(\frac{\partial \langle \mathbf{u}_\beta \rangle_\omega}{\partial y} \right)_B + (1 - \varepsilon) \left(\frac{\partial \langle \mathbf{u}_\beta \rangle_\omega}{\partial y} \right)_A \\ &= \varepsilon^2 \left(\frac{\partial \langle \mathbf{u}_\beta \rangle_\omega^\beta}{\partial y} \right)_B. \end{aligned} \quad (\text{D.8})$$

Substituting Eq. (D.8) into Eq. (D.7) leads to

$$\frac{1}{\varepsilon} \frac{\partial \langle \mathbf{u}_\beta \rangle_\omega}{\partial y} - \frac{\partial \langle \mathbf{u}_\beta \rangle_\eta}{\partial y} = \frac{\varepsilon - 1}{\mu} \mathbf{f}(u_s, K, \varepsilon). \quad (\text{D.9})$$

Due to the linearity of this flow system, this force function \mathbf{f} is also expected to have a linear expression [93]. Through dimensional

analysis, the following form has been obtained:

$$f(\mathbf{u}_s, K, \varepsilon) = \mu \cdot \gamma(\varepsilon) \cdot \frac{\mathbf{u}_s}{\sqrt{K}}, \quad (\text{D.10})$$

where $\gamma = \gamma(\varepsilon)$ is a dimensionless constant related to characteristics of the microstructures of the porous medium and is supposed to have certain relationships with porosity.

Finally, we get the stress-jump condition at the interface

$$\frac{\partial \langle \mathbf{u}_\beta \rangle_\eta}{\partial y} - \frac{1}{\varepsilon} \frac{\partial \langle \mathbf{u}_\beta \rangle_\omega}{\partial y} = (1 - \varepsilon) \cdot \gamma \cdot \frac{\mathbf{u}_s}{\sqrt{K}}. \quad (\text{D.11})$$

References

- [1] Joseph DD, Tao LN. Lubrication of a porous bearing—Stokes' solution. *J Appl Mech* 1966;33(4):753–60. <http://dx.doi.org/10.1115/1.3625178>.
- [2] Vafai K, Thiyagaraja R. Analysis of flow and heat transfer at the interface region of a porous medium. *Int J Heat Mass Transfer* 1987;30(7):1391–405. [http://dx.doi.org/10.1016/0017-9310\(87\)90171-2](http://dx.doi.org/10.1016/0017-9310(87)90171-2).
- [3] Yang K, Vafai K. Restrictions on the validity of the thermal conditions at the porous-fluid interface—An exact solution. *J Heat Transfer* 2011;133(11):112601. <http://dx.doi.org/10.1115/1.4004350>.
- [4] Cheng P, Minkowycz WJ. Free convection about a vertical flat plate embedded in a porous medium with application to heat transfer from a dike. *J Geophys Res* 1977;82(14):2040–4. <http://dx.doi.org/10.1029/jb082i014p02040>.
- [5] Liu G, Pu H, Zhao Z, Liu Y. Coupled thermo-hydro-mechanical modeling on well pairs in heterogeneous porous geothermal reservoirs. *Energy* 2019;171:631–53. <http://dx.doi.org/10.1016/j.energy.2019.01.022>.
- [6] Tsang C-F, Neretnieks I, Tsang Y. Hydrologic issues associated with nuclear waste repositories. *Water Resour Res* 2015;51(9):6923–72. <http://dx.doi.org/10.1002/2015wr017641>.
- [7] Yang Y, Wang M. Electrodifffusion of cations in compacted clay: a pore-scale view. *Environ Sci Technol* 2019;53(4):1976–84.
- [8] Bhutto AW, Bazmi AA, Zahedi G. Underground coal gasification: From fundamentals to applications. *Prog Energy Combust Sci* 2013;39(1):189–214. <http://dx.doi.org/10.1016/j.pecs.2012.09.004>.
- [9] Todd DK, Mays LW. *Groundwater hydrology*. John Wiley & Sons; 2004.
- [10] Khakpour M, Vafai K. Critical assessment of arterial transport models. *Int J Heat Mass Transfer* 2008;51(3–4):807–22. <http://dx.doi.org/10.1016/j.jheatmasstransfer.2007.04.021>.
- [11] Berman AS. Laminar flow in channels with porous walls. *J Appl Phys* 1953;24(9):1232–5. <http://dx.doi.org/10.1063/1.1721476>.
- [12] Taylor GI, Miller JCP. Fluid flow between porous rollers. *Quart J Mech Appl Math* 1956;9(2):129–35. <http://dx.doi.org/10.1093/qjmam/9.2.129>.
- [13] Beavers GS, Joseph DD. Boundary conditions at a naturally permeable wall. *J Fluid Mech* 1967;30(1):197–207. <http://dx.doi.org/10.1017/s0022112067001375>.
- [14] Saffman PG. On the boundary condition at the surface of a porous medium. *Stud Appl Math* 1971;50(2):93–101. <http://dx.doi.org/10.1002/sapm197150293>.
- [15] Richardson S. A model for the boundary condition of a porous material. Part 2. *J Fluid Mech* 1971;49(2):327–36. <http://dx.doi.org/10.1017/s002211207100209x>.
- [16] Jones IP. Low Reynolds number flow past a porous spherical shell. *Math Proc Camb Phil Soc* 1973;73(1):231–8. <http://dx.doi.org/10.1017/s0305004100047642>.
- [17] Larson RE, Higdon JLL. Microscopic flow near the surface of two-dimensional porous media. Part 1. Axial flow. *J Fluid Mech* 1986;166(-1):449–72. <http://dx.doi.org/10.1017/s0022112086000228>.
- [18] Larson RE, Higdon JLL. Microscopic flow near the surface of two-dimensional porous media. part 2. Transverse flow. *J Fluid Mech* 1987;178:119–36. <http://dx.doi.org/10.1017/s0022112087001149>.
- [19] Cao Y, Gunzburger M, Hu X, Hua F, Wang X, Zhao W. Finite element approximations for Stokes–Darcy flow with Beavers–Joseph interface conditions. *SIAM J Numer Anal* 2010;47(6):4239–56. <http://dx.doi.org/10.1137/080731542>.
- [20] Kanschat G, Rivière B. A strongly conservative finite element method for the coupling of Stokes and Darcy flow. *J Comput Phys* 2010;229(17):5933–43. <http://dx.doi.org/10.1016/j.jcp.2010.04.021>, arXiv:1712.07468.
- [21] Discacciati M, Gerardo-Giorda L. Optimized Schwarz methods for the Stokes–Darcy coupling. *IMA J Numer Anal* 2017;38(4):1959–83. <http://dx.doi.org/10.1093/imanum/drx054>.
- [22] Ahmed EN, Naqvi SB, Buda L, Bottaro A. A homogenization approach for turbulent channel flows over porous substrates: Formulation and implementation of effective boundary conditions. *Fluids* 2022;7(5):178. <http://dx.doi.org/10.3390/fluids7050178>.
- [23] Neale G, Nader W. Practical significance of brinkman's extension of darcy's law: Coupled parallel flows within a channel and a bounding porous medium. *Can J Chem Eng* 1974;52(4):475–8. <http://dx.doi.org/10.1002/cjce.5450520407>.
- [24] Poulidakos D, Kazmierczak M. Forced convection in a duct partially filled with a porous material. *J Heat Transfer* 1987;109(3):653–62. <http://dx.doi.org/10.1115/1.3248138>.
- [25] Vafai K, Kim S. Fluid mechanics of the interface region between a porous medium and a fluid layer—an exact solution. *Int J Heat Fluid Flow* 1990;11(3):254–6. [http://dx.doi.org/10.1016/0142-727x\(90\)90045-d](http://dx.doi.org/10.1016/0142-727x(90)90045-d).
- [26] James DF, Davis AMJ. Flow at the interface of a model fibrous porous medium. *J Fluid Mech* 2001;426:47–72. <http://dx.doi.org/10.1017/s0022112000002160>.
- [27] Auriault J-L. On the domain of validity of Brinkman's equation. *Transp Porous Media* 2009;79(2):215–23. <http://dx.doi.org/10.1007/s11242-008-9308-7>.
- [28] Vafai K, Tien C. Boundary and inertia effects on flow and heat transfer in porous media. *Int J Heat Mass Transfer* 1981;24(2):195–203. [http://dx.doi.org/10.1016/0017-9310\(81\)90027-2](http://dx.doi.org/10.1016/0017-9310(81)90027-2).
- [29] Breugem WP, Boersma BJ. Direct numerical simulations of turbulent flow over a permeable wall using a direct and a continuum approach. *Phys Fluids* 2005;17(2):025103. <http://dx.doi.org/10.1063/1.1835771>.
- [30] Bars ML, Worster MG. Interfacial conditions between a pure fluid and a porous medium: implications for binary alloy solidification. *J Fluid Mech* 2006;550(-1):149–73. <http://dx.doi.org/10.1017/s0022112005007998>.
- [31] Wang CY. Boundary layers in Darcy–Brinkman flow. *J Fluids Eng* 2020;143(2):024502. <http://dx.doi.org/10.1115/1.4048785>.
- [32] Zampogna GA, Bottaro A. Fluid flow over and through a regular bundle of rigid fibres. *J Fluid Mech* 2016;792:5–35. <http://dx.doi.org/10.1017/jfm.2016.66>.
- [33] Rybak I, Schwarzmeier C, Eggenweiler E, Rüde U. Validation and calibration of coupled porous-medium and free-flow problems using pore-scale resolved models. *Comput Geosci* 2021;25(2):621–35. <http://dx.doi.org/10.1007/s10596-020-09994-x>.
- [34] Eggenweiler E, Rybak I. Unsuitability of the Beavers–Joseph interface condition for filtration problems. *J Fluid Mech* 2020;892:A10. <http://dx.doi.org/10.1017/jfm.2020.194>.
- [35] Strohbeck P, Eggenweiler E, Rybak I. Computation of the Beavers–Joseph slip coefficient for coupled Stokes/Darcy problems. 2021, arXiv arXiv:2106.15556.
- [36] Hernandez-Rodriguez R, Goyeau B, Angot P, Ochoa-Tapia JA, Metropolitana UA. Average velocity profile between a fluid layer and a porous medium: Brinkman boundary layer. *Rev Mex Ing Quím* 2020;19(1):495–500. <http://dx.doi.org/10.24275/rmiq/fen843>.
- [37] Yang K, Chen H, Vafai K. Investigation of the momentum transfer conditions at the porous/free fluid interface: A benchmark solution. *Numer Heat Transfer A* 2017;71(6):609–25. <http://dx.doi.org/10.1080/10407782.2017.1293977>.
- [38] Goharzadeh A, Khalili A, Jørgensen BB. Transition layer thickness at a fluid-porous interface. *Phys Fluids* 2005;17(5):057102. <http://dx.doi.org/10.1063/1.1894796>.
- [39] Morad MR, Khalili A. Transition layer thickness in a fluid-porous medium of multi-sized spherical beads. *Exp Fluids* 2008;46(2):323. <http://dx.doi.org/10.1007/s00348-008-0562-9>.
- [40] Agelinchaab M, Tachie MF, Ruth DW. Velocity measurement of flow through a model three-dimensional porous medium. *Phys Fluids* 2006;18(1):017105. <http://dx.doi.org/10.1063/1.2164847>.
- [41] Terzis A, Zarikos I, Weishaupt K, Yang G, Chu X, Helmig R, et al. Microscopic velocity field measurements inside a regular porous medium adjacent to a low Reynolds number channel flow. *Phys Fluids* 2019;31(4):042001. <http://dx.doi.org/10.1063/1.5092169>.
- [42] Gupte SK, Advani SG. Flow near the permeable boundary of a porous medium: An experimental investigation using LDA. *Exp Fluids* 1997;22(5):408–22. <http://dx.doi.org/10.1007/s003480050067>.
- [43] Tachie MF, James DF, Currie IG. Velocity measurements of a shear flow penetrating a porous medium. *J Fluid Mech* 2003;493:319–43. <http://dx.doi.org/10.1017/s0022112003005986>.
- [44] Ochoa-Tapia J, Valdès-Parada F, Goyeau B, Lasseux D. Fluid motion in the fluid/porous medium inter-region. *Rev Mex Ing Quím* 2017.
- [45] Okabe H, Blunt MJ. Prediction of permeability for porous media reconstructed using multiple-point statistics. *Phys Rev E* 2004;70:066135. <http://dx.doi.org/10.1103/PhysRevE.70.066135>, URL: <https://link.aps.org/doi/10.1103/PhysRevE.70.066135>.
- [46] Hosseini M, Siavashi M, Shirbani M, Nezhad MM. Reliability assessment of the lattice-Boltzmann method for modeling and quantification of hydrological attributes of porous media from microtomography images. *Adv Water Resour* 2023;171:104351. <http://dx.doi.org/10.1016/j.advwatres.2022.104351>.
- [47] Chen S, Doolen GD. Lattice Boltzmann method for fluid flows. *Annu Rev Fluid Mech* 1998;30:329–64.
- [48] Krüger T, Kusumaatmaja H, Kuzmin A, Shardt O, Silva G, Viggen EM. The lattice Boltzmann method, principles and practice. *Grad Texts Phys* 2016;105–52. http://dx.doi.org/10.1007/978-3-319-44649-3_4.
- [49] Parmigiani A, Huber C, Bachmann O, Chopard B. Pore-scale mass and reactant transport in multiphase porous media flows. *J Fluid Mech* 2011;686:40–76. <http://dx.doi.org/10.1017/jfm.2011.268>.
- [50] Wang Z, Wang M, Chen S. Coupling of high Knudsen number and non-ideal gas effects in microporous media. *J Fluid Mech* 2018;840:56–73. <http://dx.doi.org/10.1017/jfm.2018.46>.
- [51] Xian W, Takayuki A. Multi-GPU performance of incompressible flow computation by lattice Boltzmann method on GPU cluster. *Parallel Comput* 2011;37(9):521–35. <http://dx.doi.org/10.1016/j.parco.2011.02.007>.

- [52] Xie C, Raecini AQ, Wang Y, Blunt MJ, Wang M. An improved pore-network model including viscous coupling effects using direct simulation by the lattice Boltzmann method. *Adv Water Resour* 2017;100:26–34. <http://dx.doi.org/10.1016/j.advwatres.2016.11.017>, URL: <https://www.sciencedirect.com/science/article/pii/S0309170816302925>.
- [53] Angot P, Goyeau B, Ochoa-Tapia JA. Asymptotic modeling of transport phenomena at the interface between a fluid and a porous layer: Jump conditions. *Phys Rev E* 2017;95(6):063302. <http://dx.doi.org/10.1103/physreve.95.063302>.
- [54] Ochoa-Tapia J, Whitaker S. Momentum transfer at the boundary between a porous medium and a homogeneous fluid—I. Theoretical development. *Int J Heat Mass Transfer* 1995;38(14):2635–46. [http://dx.doi.org/10.1016/0017-9310\(94\)00346-w](http://dx.doi.org/10.1016/0017-9310(94)00346-w).
- [55] Basu AJ, Khalili A. Computation of flow through a fluid-sediment interface in a benthic chamber. *Phys Fluids* 1999;11(6):1395–405. <http://dx.doi.org/10.1063/1.870004>.
- [56] Valdés-Parada FJ, Lasseux D. Flow near porous media boundaries including inertia and slip: A one-domain approach. *Phys Fluids* 2021;33(7):073612. <http://dx.doi.org/10.1063/5.0056345>.
- [57] Eggenweiler E, Rybak I. Effective coupling conditions for arbitrary flows in Stokes–Darcy systems. *Multiscale Model Simul* 2021;19(2):731–57. <http://dx.doi.org/10.1137/20m1346638>.
- [58] Jäger W, Mikelić A, Neuss N. Asymptotic analysis of the laminar viscous flow over a porous bed. *SIAM J Sci Comput* 2001;22(6):2006–28. <http://dx.doi.org/10.1137/s1064827599360339>.
- [59] Lyu W, Wang X. Stokes–Darcy system, small-Darcy-number behaviour and related interfacial conditions. *J Fluid Mech* 2021;922:A4. <http://dx.doi.org/10.1017/jfm.2021.509>.
- [60] Sudhakar Y, Lācis U, Pasche S, Bagheri S. Higher-order homogenized boundary conditions for flows over rough and porous surfaces. *Transp Porous Media* 2021;136(1):1–42. <http://dx.doi.org/10.1007/s11242-020-01495-w>, arXiv:1909.07125.
- [61] Naqvi SB, Bottaro A. Interfacial conditions between a free-fluid region and a porous medium. *Int J Multiph Flow* 2021;141:103585. <http://dx.doi.org/10.1016/j.ijmultiphaseflow.2021.103585>.
- [62] Whitaker S. Flow in porous media I: A theoretical derivation of Darcy's law. *Transp Porous Media* 1986;1(1):3–25. <http://dx.doi.org/10.1007/bf01036523>.
- [63] Goyeau B, Luillier D, Gobin D, Velarde M. Momentum transport at a fluid-porous interface. *Int J Heat Mass Transfer* 2003;46(21):4071–81. [http://dx.doi.org/10.1016/s0017-9310\(03\)00241-2](http://dx.doi.org/10.1016/s0017-9310(03)00241-2).
- [64] Deng C, Martínez D. Viscous flow in a channel partially filled with a porous medium and with wall suction. *Chem Eng Sci* 2005;60(2):329–36. <http://dx.doi.org/10.1016/j.ces.2004.08.010>.
- [65] Quintard M, Whitaker S. Transport in ordered and disordered porous media II: Generalized volume averaging. *Transp Porous Media* 1994;14(2):179–206. <http://dx.doi.org/10.1007/bf00615200>.
- [66] Alberto J. Momentum jump condition at the boundary between a porous medium and a homogeneous fluid: inertial effects. *J Porous Media* 1998;1(3):201–17.
- [67] Wang M, Wang J, Pan N, Chen S. Mesoscopic predictions of the effective thermal conductivity for microscale random porous media. *Phys Rev E* 2007;75(3):036702. <http://dx.doi.org/10.1103/physreve.75.036702>.
- [68] Wang M, Pan N. Elastic property of multiphase composites with random microstructures. *J Comput Phys* 2009;228:5978–88.
- [69] Gostick JT, Khan ZA, Tranter TG, Kok MD, Agnaou M, Sadeghi M, et al. PoreSpy: A Python toolkit for quantitative analysis of porous media images. *J Open Source Softw* 2019;4(37):1296. <http://dx.doi.org/10.21105/joss.01296>.
- [70] Wang J, Chen L, Kang Q, Rahman SS. The lattice Boltzmann method for isothermal micro-gaseous flow and its application in shale gas flow: A review. *Int J Heat Mass Transfer* 2016;95:94–108. <http://dx.doi.org/10.1016/j.ijheatmasstransfer.2015.12.009>.
- [71] Ghasemi K, Siavashi M. Three-dimensional analysis of magnetohydrodynamic transverse mixed convection of nanofluid inside a lid-driven enclosure using MRT-LBM. *Int J Mech Sci* 2020;165:105199. <http://dx.doi.org/10.1016/j.ijmeosci.2019.105199>.
- [72] Khirevich S, Ginzburg I, Tallarek U. Coarse- and fine-grid numerical behavior of MRT/TRT lattice-Boltzmann schemes in regular and random sphere packings. *J Comput Phys* 2015;281:708–42. <http://dx.doi.org/10.1016/j.jcp.2014.10.038>.
- [73] Zou Q, He X. On pressure and velocity boundary conditions for the lattice Boltzmann BGK model. *Phys Fluids* 1997;9(6):1591–8. <http://dx.doi.org/10.1063/1.869307>, arXiv:comp-gas/9611001.
- [74] Zhang J, Kwok DY. Pressure boundary condition of the lattice Boltzmann method for fully developed periodic flows. *Phys Rev E* 2006;73(4):047702. <http://dx.doi.org/10.1103/physreve.73.047702>.
- [75] Hecht M, Harting J. Implementation of on-site velocity boundary conditions for D3Q19 lattice Boltzmann simulations. *J Stat Mech Theory Exp* 2010;2010(01):P01018. <http://dx.doi.org/10.1088/1742-5468/2010/01/p01018>, arXiv:0811.4593.
- [76] Xu Z, Zhang J, Young Y-N, Yue P, Feng JJ. Comparison of four boundary conditions for the fluid-hydrogel interface. *Phys Rev Fluids* 2022;7(9):093301. <http://dx.doi.org/10.1103/physrevfluids.7.093301>.
- [77] Valdés-Parada FJ, Aguilar-Madera CG, Ochoa-Tapia JA, Goyeau B. Velocity and stress jump conditions between a porous medium and a fluid. *Adv Water Resour* 2013;62:327–39. <http://dx.doi.org/10.1016/j.advwatres.2013.08.008>.
- [78] Lācis U, Bagheri S. A framework for computing effective boundary conditions at the interface between free fluid and a porous medium. *J Fluid Mech* 2017;812:866–89. <http://dx.doi.org/10.1017/jfm.2016.838>, arXiv:1604.02880.
- [79] Beavers GS, Sparrow EM, Magnuson RA. Experiments on coupled parallel flows in a channel and a bounding porous medium. *J Basic Eng* 1970;92(4):843–8. <http://dx.doi.org/10.1115/1.3425155>.
- [80] Valdés-Parada FJ, Goyeau B, Ochoa-Tapia JA. Jump momentum boundary condition at a fluid-porous dividing surface: Derivation of the closure problem. *Chem Eng Sci* 2007;62(15):4025–39. <http://dx.doi.org/10.1016/j.ces.2007.04.042>.
- [81] Nabovati A, Amon CH. Hydrodynamic boundary condition at open-porous interface: A pore-level lattice Boltzmann study. *Transp Porous Media* 2013;96(1):83–95. <http://dx.doi.org/10.1007/s11242-012-0074-1>.
- [82] Rashidi S, Nouri-Borujerdi A, Valipour MS, Ellahi R, Pop I. Stress-jump and continuity interface conditions for a cylinder embedded in a porous medium. *Transp Porous Media* 2015;107(1):171–86. <http://dx.doi.org/10.1007/s11242-014-0431-3>.
- [83] Chen H, Wang J, Yang K. Analysis of the momentum transport boundary conditions at a fluid-porous interface. 2016. http://dx.doi.org/10.1115/ht2016-7395_V001T03A006-V001T03A006.
- [84] Whitaker S. The Forchheimer equation: A theoretical development. *Transp Porous Media* 1996;25(1):27–61. <http://dx.doi.org/10.1007/bf00141261>.
- [85] Valdés-Parada FJ, Lasseux D. A novel one-domain approach for modeling flow in a fluid-porous system including inertia and slip effects. *Phys Fluids* 2021;33(2):022106. <http://dx.doi.org/10.1063/5.0036812>.
- [86] Brinkman HC. A calculation of the viscous force exerted by a flowing fluid on a dense swarm of particles. *Flow Turbul Combust* 1949;1(1):27. <http://dx.doi.org/10.1007/bf02120313>.
- [87] Wu Z, Mirbod P. Experimental analysis of the flow near the boundary of random porous media. *Phys Fluids* 2018;30(4):047103. <http://dx.doi.org/10.1063/1.5021903>.
- [88] Chapman AM, Higdon JLL. Oscillatory Stokes flow in periodic porous media. *Physics Fluids A* 1992;4(10):2099–116. <http://dx.doi.org/10.1063/1.858507>.
- [89] Eshghinejadfard A, Daróczy L, Janiga G, Thévenin D. Calculation of the permeability in porous media using the lattice Boltzmann method. *Int J Heat Fluid Flow* 2016;62:93–103. <http://dx.doi.org/10.1016/j.ijheatfluidflow.2016.05.010>.
- [90] Sahraoui M, Kaviani M. Slip and no-slip velocity boundary conditions at interface of porous, plain media. *Int J Heat Mass Transfer* 1992;35(4):927–43. [http://dx.doi.org/10.1016/0017-9310\(92\)90258-t](http://dx.doi.org/10.1016/0017-9310(92)90258-t).
- [91] Ochoa-Tapia J, Whitaker S. Momentum transfer at the boundary between a porous medium and a homogeneous fluid—II. Comparison with experiment. *Int J Heat Mass Transfer* 1995;38(14):2647–55. [http://dx.doi.org/10.1016/0017-9310\(94\)00347-x](http://dx.doi.org/10.1016/0017-9310(94)00347-x).
- [92] Howes FA, Whitaker S. The spatial averaging theorem revisited. *Chem Eng Sci* 1985;40(8):1387–92. [http://dx.doi.org/10.1016/0009-2509\(85\)80078-6](http://dx.doi.org/10.1016/0009-2509(85)80078-6).
- [93] Broens M, Unsal E. Emulsification kinetics during quasi-miscible flow in dead-end pores. *Adv Water Resour* 2018;113:13–22. <http://dx.doi.org/10.1016/j.advwatres.2018.01.001>.